Available online at www.sciencedirect.com
ScienceDirect
Journal of Computational Physics 220 (2007) 791–812
JOURNAL OF COMPUTATIONAL PHYSICS
www.elsevier.com/locate/jcp

An adaptive moving mesh method for two-dimensional ideal magnetohydrodynamics

Jianqiang Han, Huazhong Tang *

LMAM, School of Mathematical Sciences, Peking University, 5# YiHe Yuan Lu, Haidian District, Beijing 100871, PR China

Received 15 June 2005; received in revised form 5 April 2006; accepted 23 May 2006
Available online 10 July 2006

Abstract

This paper presents an adaptive moving mesh algorithm for two-dimensional (2D) ideal magnetohydrodynamics (MHD) that utilizes a staggered constrained transport technique to keep the magnetic field divergence-free. The algorithm consists of two independent parts: MHD evolution and mesh-redistribution. The first part is a high-resolution, divergence-free, shock-capturing scheme on a fixed quadrangular mesh, while the second part is an iterative procedure. In each iteration, mesh points are first redistributed, and then a conservative-interpolation formula is used to calculate the remapped cell-averages of the mass, momentum, and total energy on the resulting new mesh; the magnetic potential is remapped to the new mesh in a non-conservative way and is reconstructed to give a divergence-free magnetic field on the new mesh. Several numerical examples are given to demonstrate that the proposed method can achieve high numerical accuracy, track and resolve strong shock waves in ideal MHD problems, and preserve divergence-free property of the magnetic field. Numerical examples include the smooth Alfvén wave problem, 2D and 2.5D shock tube problems, two rotor problems, the stringent blast problem, and the cloud–shock interaction problem.

Keywords: Adaptive moving mesh method; Finite volume method; Constrained transport; Magnetohydrodynamics; Divergence-free

1. Introduction

The governing equations of two-dimensional (2D) ideal magnetohydrodynamics (MHD) may be written in a conservative form as follows:

$$\frac{\partial \rho}{\partial t} + \nabla \cdot (\rho \boldsymbol{u}) = 0, \tag{1.1}$$

$$\frac{\partial \rho \boldsymbol{u}}{\partial t} + \nabla \cdot (\rho \boldsymbol{u}\boldsymbol{u} - \boldsymbol{B}\boldsymbol{B}) + \nabla p_{\text{tot}} = 0, \tag{1.2}$$

* Corresponding author. Tel.: +86 10 62757018; fax: +86 10 62751801.
E-mail addresses: jqhan@pku.edu.cn (J. Han), hztang@math.pku.edu.cn (H. Tang).

0021-9991/$ - see front matter © 2006 Elsevier Inc. All rights reserved.
doi:10.1016/j.jcp.2006.05.031

$$\frac{\partial E}{\partial t} + \nabla \cdot (\boldsymbol{u}E + \boldsymbol{u}p_{\text{tot}} - \boldsymbol{B}(\boldsymbol{B} \cdot \boldsymbol{u})) = 0, \tag{1.3}$$

$$\frac{\partial \boldsymbol{B}}{\partial t} + \nabla \cdot (\boldsymbol{u}\boldsymbol{B} - \boldsymbol{B}\boldsymbol{u}) = 0, \tag{1.4}$$

where ρ, p_{tot}, $\boldsymbol{u} = (u_1, u_2, u_3)^{\text{T}}$, and $\boldsymbol{B} = (B_1, B_2, B_3)^{\text{T}}$ denote the gas mass density, the total pressure containing the gas and magnetic pressures: $p_{\text{tot}} = p + p_{\text{mag}}$, the fluid velocity vector, and the magnetic field, respectively. The magnetic pressure is defined by

$$p_{\text{mag}} = \frac{1}{2}\boldsymbol{B} \cdot \boldsymbol{B}.$$

The total energy E consists of thermal, kinetic, and magnetic energies

$$E = \rho e + \frac{1}{2}(\rho \boldsymbol{u} \cdot \boldsymbol{u} + \boldsymbol{B} \cdot \boldsymbol{B}), \tag{1.5}$$

where e denotes the thermal energy density. For ideal gases, the thermal energy is related to the gas pressure through the equation of state

$$p = (\gamma - 1)\rho e, \tag{1.6}$$

where γ is the adiabatic index or the ratio of the specific heats.

Eqs. (1.1)–(1.4) represent conservation of the gas mass, momentum, total energy, and magnetic field, respectively, and are combined with (1.5) and (1.6) to form a closed system. Solutions of the MHD equations must also satisfy a divergence-free constraint on the magnetic field, that is

$$\nabla \cdot \boldsymbol{B} = 0, \tag{1.7}$$

if the initial magnetic field is divergence-free. It is imposed by Maxwell's equations.

The ideal MHD equations are very important in modelling phenomena in a wide range of applications including space weather, laboratory plasmas, solar physics, and astrophysical fluid flows etc. In the past two decades, various high-resolution schemes have been developed for the MHD equations. Most of these schemes are based on approximate Riemann solvers where seven or eight-wave family eigen-system is applied to the characteristic decomposition. We refer the readers to the literatures, see e.g. [1,5,6,12,18,26,27,34,36,41,46]. Comparisons of some flux corrected transport and total variation diminishing numerical schemes as well as various constrained transport methods for MHD problems are given by Tóth and Odstrcil in [53,52]. Due to the non-strictly hyperbolicity of the MHD system, considerable work is required for validation of the MHD eigen-system. Based on the particle transport mechanism, Croisille et al. and Xu et al. constructed gas-kinetic MHD solvers [16,57,49]. Because of the simplicity of kinetic flux functions, the efficiency becomes one of the advantages in the kinetic approach. Study of adaptive mesh methods for the MHD equations has attracted some researchers' attention. Strauss and Longcope proposed an adaptive finite element method for MHD system [44]. Divergence-free adaptive mesh refinement methods were studied in [5,28].

The main difficulty in multidimensional MHD calculations is to handle the divergence-free constraint. Violating this constraint leads to non-physical plasma transport orthogonal to the magnetic field. Up to now, there are three rather popular approaches to treat this difficulty. The first approach is the projection method of Brackbill and Barnes [10]. In order to impose the divergence-free condition for the magnetic field, a correction method is enforced in solving the Poisson equation for the potential ϕ, such as $\nabla^2\phi + \nabla \cdot \boldsymbol{B} = 0$, to obtain the corrected magnetic field $\boldsymbol{B}^c$ through $\boldsymbol{B}^c = \boldsymbol{B} + \nabla\phi$, where $\boldsymbol{B}$ is given by numerically solving the MHD equations and does not satisfy the divergence-free constraint, while $\boldsymbol{B}^c$ is divergence-free and used in the next time step. This technique is commonly used in many MHD solvers [10,25,58,49]. However, in general, the Poisson solver is time consuming on non-rectangular meshes.

The second approach is the eight-wave formulation of the MHD equations suggested by Powell [35], who added source terms $-(\nabla \cdot \boldsymbol{B})\boldsymbol{B}$, $-(\nabla \cdot \boldsymbol{B})(\boldsymbol{B} \cdot \boldsymbol{u})$, and $-(\nabla \cdot \boldsymbol{B})\boldsymbol{u}$ to the right hand side of the ideal MHD equations (1.2)–(1.4), respectively. The main disadvantage of this approach is that the 8-wave formulation of the MHD equations becomes non-conservative so that incorrect results may be produced in problems involving strong shocks, see [52].

The third approach is the constrained transport (CT) method of Evans and Hawley [22], in which a particular finite difference method was constructed on a staggered mesh, maintaining a specific discretization of $\nabla \cdot \boldsymbol{B}$. Because of its simplicity, this approach becomes rather popular in recent years, see e.g. [7,17,39]. Tóth [52] introduced a finite-volume interpretation of the CT schemes that place all of the variables at the cell center. However, it seems to be difficultly applied to an adaptive mesh (refinement mesh or moving mesh). It is worth noting that most of the existing CT methods are designed on a rectangle or cubic mesh. Another way to keep the magnetic field divergence-free is to directly solve the magnetic potential equations instead of the induction equation (1.4), see [15,22,38]. The disadvantage of this approach is that the order of spatial derivatives increases by one, which leads to the reduction of the order of accuracy by one. To avoid the decrease of accuracy, we should use a higher order polynomial to approximate the magnetic potential than that used for the fluid variables. We shall show below that its 2D implementation is convenient, and a higher-order accurate approximation can be achieved on an adaptive moving mesh.

Adaptive moving mesh methods have important applications for a variety of scientific and engineering areas such as solid and fluid dynamics etc., where singular or nearly singular solutions are developed dynamically in fairly localized regions of shock waves, boundary layers, and detonation waves etc. Numerically investigating these phenomena require extremely fine meshes over a small portion of the physical domain to resolve the large solution variations. Successful implementation of an adaptive strategy can increase accuracy of the numerical approximations and decrease the computational cost. Up to now, there have been many important progresses in adaptive moving mesh methods for partial differential equations (PDE), including grid redistribution approach based on the variational principle of Winslow [56], Brackbill [9], Brackbill and Saltzman [11], Ren and Wang [37], and Wang and Wang [55]; moving finite element methods of Millers [33], and Davis and Flaherty [19]; moving mesh PDEs methods of Russell et al. [13,43], and Li and Petzold [29], and Ceniceros and Hou [14]; and moving mesh methods based on the harmonic mapping of Dvinsky [21], and Li et al. [30,31,20]. Computational costs of moving mesh methods can be efficiently saved with locally varying time steps [45]. We also refer the readers to a recent review paper [50] and references therein.

The main objective of this paper is to extend adaptive moving mesh methods developed in [47] to the MHD equations (1.1)–(1.4) in the two-dimensional case. The key is to keep the magnetic field divergence-free and fluid variables, such as the mass, momentum, and total energy, conservative. Harten and Hyman [24] began the earliest study of adaptive moving mesh methods for hyperbolic problems by moving the grid at an adaptive speed in each time step to improve the resolution of shocks and contact discontinuities. After their work, many other moving mesh methods for hyperbolic problems have been proposed in the literatures, including Azarenok et al. [2–4], Fazio and LeVeque [23], Liu et al. [32], Saleri and Steinberg [40], Stockie et al. [43], and Tang et al. [47,48]. The algorithms developed in [47,48] are formed by two independent parts: PDE evolution and mesh-redistribution. The "mass"-conservation of the underlying numerical solutions is kept at each solution remapping step. For ideal MHD equations, we shall employ a staggered CT technique to further get the divergence-free magnetic field.

The paper is organized as follows. Section 2 introduces divergence-free finite volume methods of ideal MHD equations on an arbitrary quadrangular mesh that utilize a staggered CT technique to keep the magnetic field divergence-free. Section 3 proposes the adaptive moving mesh algorithm for system of ideal MHD equations. The conservative and non-conservative re-mapping approaches are respectively applied to the conservative fluid variables and the magnetic potential. Full solution procedure will be outlined in Section 4, ending with several remarks. Numerical experiments are carried out in Section 5 on several benchmark examples, which are the smooth Alfvén wave problem, 2D and 2.5D oblique shock-tube problems, the rotor problem, the stringent blast problem, and cloud–shock interaction problem. Finally, we conclude this work by giving a few remarks in Section 6.

2. Numerical methods for the MHD equations

In this section, we introduce a divergence-free finite volume approximation of the MHD equations (1.1)–(1.4) on a fixed quadrangular mesh, but we restrict our attention to two-dimensional case and the structured quadrangular mesh throughout this paper. The system (1.1)–(1.4) may be rewritten in a compact form as follows:

$$\frac{\partial \boldsymbol{U}}{\partial t}+\sum_{i=1}^{2}\frac{\partial \boldsymbol{F}_i(\boldsymbol{U})}{\partial x_i}=0, \tag{2.1}$$

where $(x_1,x_2)=(x,y):=\boldsymbol{x}$ denote the spatial coordinates in the physical domain Ω_p, and the conservative variables $\boldsymbol{U}$ and the fluxes $\boldsymbol{F}_i(\boldsymbol{U})$ along x_i-direction, $i=1,2$, have explicit forms as

$$\begin{aligned}
\boldsymbol{U} &= (\rho,\rho u_1,\rho u_2,\rho u_3,B_1,B_2,B_3,E)^{\mathrm{T}},\\
\boldsymbol{F}_1 &= (\rho u_1,\rho u_1^2+p_{\mathrm{tot}}-B_1^2,\rho u_1u_2-B_1B_2,\rho u_1u_3-B_1B_3,0,u_1B_2-u_2B_1,\\
&\quad u_1B_3-u_3B_1,u_1(E+p_{\mathrm{tot}})-B_1(\boldsymbol{u}\cdot\boldsymbol{B}))^{\mathrm{T}},\\
\boldsymbol{F}_2 &= (\rho u_2,\rho u_1u_2-B_1B_2,\rho u_2^2+p_{\mathrm{tot}}-B_2^2,\rho u_2u_3-B_2B_3,u_2B_1-u_1B_2,0,\\
&\quad u_2B_3-u_3B_2,u_2(E+p_{\mathrm{tot}})-B_2(\boldsymbol{u}\cdot\boldsymbol{B}))^{\mathrm{T}}.
\end{aligned}$$

It is easy to know that the exact magnetic field $\boldsymbol{B}$ is divergence-free when the initial data satisfy $\nabla\cdot\boldsymbol{B}|_{t=0}=0$. To preserve the divergence-free property in the numerical level, following the ideas of Clarke, and Evans and Hawley [15,22], we define uniquely a vector potential $\mathscr{A}=(0,0,\mathscr{A})^{\mathrm{T}}$ by

$$\boldsymbol{B}=\nabla\times\mathscr{A}, \tag{2.2}$$

and the Coulomb gauge $\nabla\cdot\mathscr{A}=0$.

From (1.4), we have

$$\frac{\partial\mathscr{A}}{\partial t}+\Omega=0, \tag{2.3}$$

where Ω is the x_3-component of the electric field $\boldsymbol{\Omega}=\boldsymbol{B}\times\boldsymbol{u}$, which is Ohm's law for a perfect conductor. The magnetic potential can also be evolved by an equivalent form of

$$\frac{\partial\mathscr{A}}{\partial t}+u_1\frac{\partial\mathscr{A}}{\partial x_1}+u_2\frac{\partial\mathscr{A}}{\partial x_2}=0. \tag{2.4}$$

Once the magnetic potential $\mathscr{A}$ is known, the magnetic field calculated from (2.2) will be divergence-free.

In numerical computations, we still need eigenvalues of Jacobian matrix of the fluxes $\boldsymbol{F}_i$, $i=1,2$. For example, eigenvalues of $\partial\boldsymbol{F}_1/\partial\boldsymbol{U}$ are

$$\begin{aligned}
&\lambda_1=u_1-c_f,\quad \lambda_2=u_1-c_a,\quad \lambda_3=u_1-c_s,\quad \lambda_4=u_1,\\
&\lambda_5=u_1+c_s,\quad \lambda_6=u_1+c_a,\quad \lambda_7=u_1+c_f,
\end{aligned}$$

where the fast and slow speeds, c_f and c_s, are defined by

$$\begin{aligned}
c_f &= \left(\frac{1}{2}(a^2+b^2+\sqrt{(a^2+b^2)^2-4a^2B_1^2/\rho})\right)^{\frac{1}{2}},\\
c_s &= \left(\frac{1}{2}(a^2+b^2-\sqrt{(a^2+b^2)^2-4a^2B_1^2/\rho})\right)^{\frac{1}{2}},
\end{aligned}$$

here the sound speed $a^2=\gamma p/\rho$, the Alfvén speed $c_a=|B_1|/\sqrt{\rho}$, and $b^2=(\boldsymbol{B}\cdot\boldsymbol{B})/\rho$.

2.1. The base scheme

Given a partition of the physical domain Ω_p, $\{A_{j+\frac{1}{2},k+\frac{1}{2}}|j,k\in\mathbb{Z}\}$, and a partition of the time interval $[0,T]$, $\{t_n=t_{n-1}+\Delta t_n|\Delta t_n>0,\ n=1,\ldots\}$, where $A_{j+\frac{1}{2},k+\frac{1}{2}}$ is a quadrangle with four corners $\boldsymbol{x}_{j,k},\boldsymbol{x}_{j+1,k},\boldsymbol{x}_{j+1,k+1}$, and $\boldsymbol{x}_{j,k+1}$, see Fig. 1. We begin to describe the base scheme in details. Similar to the staggered CT method of Evans and Hawley [22], the variables ρ, $\rho\boldsymbol{u}$, E and $\boldsymbol{B}$ are approximated at cell centers by their cell averages

$$\boldsymbol{U}_{j+\frac{1}{2},k+\frac{1}{2}}(t)=\frac{1}{|A_{j+\frac{1}{2},k+\frac{1}{2}}|}\int_{A_{j+\frac{1}{2},k+\frac{1}{2}}}\boldsymbol{U}(\boldsymbol{x},t)\,\mathrm{d}\boldsymbol{x}, \tag{2.5}$$

where $|A_{j+\frac{1}{2},k+\frac{1}{2}}|$ denotes the area of the control volume $A_{j+\frac{1}{2},k+\frac{1}{2}}$. The magnetic potential $\mathscr{A}$ and the electric field Ω are discretized at the cell corners.

We further denote $\boldsymbol{U}^n_{j+\frac{1}{2},k+\frac{1}{2}}$ as an approximation of $\boldsymbol{U}_{j+\frac{1}{2},k+\frac{1}{2}}(t_n)$ and reconstruct a polynomial approximation of $\boldsymbol{U}$ within each control volume, for instance, a linear polynomial as follows:

$$\boldsymbol{U}_{A_{j+\frac{1}{2},k+\frac{1}{2}}}(\boldsymbol{x},t_n)=\boldsymbol{U}^n_{j+\frac{1}{2},k+\frac{1}{2}}+\boldsymbol{S}^n_{j+\frac{1}{2},k+\frac{1}{2}}\cdot(\boldsymbol{x}-\boldsymbol{x}_{j+\frac{1}{2},k+\frac{1}{2}}),\quad \boldsymbol{x}\in A_{j+\frac{1}{2},k+\frac{1}{2}},\tag{2.6}$$

where $\boldsymbol{S}$ denotes an approximation of the gradient vector $\nabla_{\boldsymbol{x}}\boldsymbol{U}=(\frac{\partial \boldsymbol{U}}{\partial x},\frac{\partial \boldsymbol{U}}{\partial y})^{\mathrm{T}}$ by using a nonlinear limiter function, and $\boldsymbol{x}_{j+\frac{1}{2},k+\frac{1}{2}}$ denotes the centroid of $A_{j+\frac{1}{2},k+\frac{1}{2}}$. The van Leer limiter [54] is applied in our computations and implemented as follows. If we use S^x and S^y to denote x- and y- components of $\boldsymbol{S}$, they are computed as

$$\begin{aligned}
S^x_{j+\frac{1}{2},k+\frac{1}{2}}&=(\xi_x)_{j+\frac{1}{2},k+\frac{1}{2}}S^{\xi}_{j+\frac{1}{2},k+\frac{1}{2}}+S^{\eta}_{j+\frac{1}{2},k+\frac{1}{2}}(\eta_x)_{j+\frac{1}{2},k+\frac{1}{2}},\\
S^y_{j+\frac{1}{2},k+\frac{1}{2}}&=(\xi_y)_{j+\frac{1}{2},k+\frac{1}{2}}S^{\xi}_{j+\frac{1}{2},k+\frac{1}{2}}+S^{\eta}_{j+\frac{1}{2},k+\frac{1}{2}}(\eta_y)_{j+\frac{1}{2},k+\frac{1}{2}},
\end{aligned}$$

with

$$\begin{aligned}
S^{\xi}_{j+\frac{1}{2},k+\frac{1}{2}}&=\frac{1}{\Delta\xi}\mathrm{vLL}\Big(\boldsymbol{U}_{j+\frac{1}{2},k+\frac{1}{2}}-\boldsymbol{U}_{j-\frac{1}{2},k+\frac{1}{2}},\boldsymbol{U}_{j+\frac{3}{2},k+\frac{1}{2}}-\boldsymbol{U}_{j+\frac{1}{2},k+\frac{1}{2}}\Big),\\
S^{\eta}_{j+\frac{1}{2},k+\frac{1}{2}}&=\frac{1}{\Delta\eta}\mathrm{vLL}\Big(\boldsymbol{U}_{j+\frac{1}{2},k+\frac{1}{2}}-\boldsymbol{U}_{j+\frac{1}{2},k-\frac{1}{2}},\boldsymbol{U}_{j+\frac{1}{2},k+\frac{3}{2}}-\boldsymbol{U}_{j+\frac{1}{2},k+\frac{1}{2}}\Big),
\end{aligned}$$

where $\xi_x=y_\eta/J$, $\xi_y=-x_\eta/J$, $\eta_x=-y_\xi/J$ and $\eta_y=x_\xi/J$, $J=x_\xi y_\eta-x_\eta y_\xi$, and they are approximated by second order central differences. The function $\mathrm{vLL}(a,b)$ denotes van Leer's limiter defined as

$$\mathrm{vLL}(a,b)=(\mathrm{sign}(a)+\mathrm{sign}(b))\frac{|ab|}{|a|+|b|+\varepsilon},$$

where the parameter ε, $0<\varepsilon\ll 1$, is used to avoid that the denominator becomes zero.

Remark 2.1. In practical computations, we may simply use the initial data reconstruction in the logical space instead of that in the physical space (2.6), that is,

$$\boldsymbol{U}_{A_{j+\frac{1}{2},k+\frac{1}{2}}}(\boldsymbol{\xi},t_n)=\boldsymbol{U}^n_{j+\frac{1}{2},k+\frac{1}{2}}+\boldsymbol{S}^{\boldsymbol{\xi},n}_{j+\frac{1}{2},k+\frac{1}{2}}\cdot(\boldsymbol{\xi}-\boldsymbol{\xi}_{j+\frac{1}{2},k+\frac{1}{2}}),\tag{2.7}$$

where $\xi_j<\xi<\xi_{j+1}$, $\eta_k<\eta<\eta_{k+1}$, $\boldsymbol{S}^{\boldsymbol{\xi}}_{j+\frac{1}{2},k+\frac{1}{2}}=(S^{\xi},S^{\eta})^{\mathrm{T}}$ is an approximation of $\nabla_{\boldsymbol{\xi}}\boldsymbol{U}=(\frac{\partial \boldsymbol{U}}{\partial \xi},\frac{\partial \boldsymbol{U}}{\partial \eta})^{\mathrm{T}}$.

Remark 2.2. The magnetic field $\boldsymbol{B}_{A_{j+\frac{1}{2},k+\frac{1}{2}}}(\boldsymbol{x},t_n)$ satisfying $\nabla\cdot\boldsymbol{B}=0$ in $A_{j+\frac{1}{2},k+\frac{1}{2}}$ will be computed from the reconstructed magnetic potential, see Section 2.2, rather than (2.6) or (2.7).

Integrating (2.1) over the control volume $A_{j+\frac{1}{2},k+\frac{1}{2}}$ and using the divergence theorem, we obtain

$$|A_{j+\frac{1}{2},k+\frac{1}{2}}|\frac{\mathrm{d}}{\mathrm{d}t}\boldsymbol{U}_{j+\frac{1}{2},k+\frac{1}{2}}(t)+\sum_{i=1}^{4}\int_{L^i}\boldsymbol{F}_{n^i}(\boldsymbol{U})\,\mathrm{d}l=0,\tag{2.8}$$

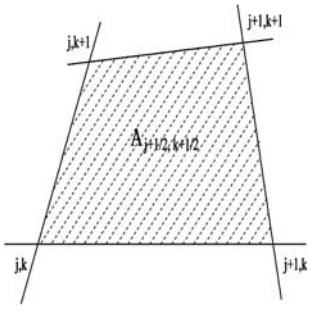

Fig. 1. A control volume.

where $\boldsymbol{F}_{n^i} = \boldsymbol{F}_1 n_1^i + \boldsymbol{F}_2 n_2^i$, $\boldsymbol{n}^i = (n_1^i, n_2^i)$ denotes the outward unit normal vector on the ith edge L^i of the control volume $A_{j+\frac{1}{2},k+\frac{1}{2}}$, $i = 1,\ldots,4$. To get a second order approximation, we simply discretize (2.8) in space and obtain the following ordinary differential equation system:

$$\frac{\mathrm{d}}{\mathrm{d}t}\boldsymbol{U}_{j+\frac{1}{2},k+\frac{1}{2}}(t) = -\frac{1}{|A_{j+\frac{1}{2},k+\frac{1}{2}}|}\sum_{i=1}^{4}\widehat{\boldsymbol{F}}_{n^i}(\boldsymbol{U}_L,\boldsymbol{U}_R)|L^i|, \tag{2.9}$$

where the numerical flux $\widehat{\boldsymbol{F}}_{n^i}(\boldsymbol{U}_L,\boldsymbol{U}_R)$ may be written in a viscosity form of

$$\widehat{\boldsymbol{F}}_{n^i}(\boldsymbol{U}_L,\boldsymbol{U}_R) = \frac{1}{2}(\boldsymbol{F}_{n^i}(\boldsymbol{U}_L) + \boldsymbol{F}_{n^i}(\boldsymbol{U}_R) - \boldsymbol{Q}^i\cdot(\boldsymbol{U}_R - \boldsymbol{U}_L)), \tag{2.10}$$

which may be derived by a local 1D approximate or exact Riemann solver, see e.g. [51]. Here $\boldsymbol{Q}^i = \boldsymbol{Q}^i(\boldsymbol{U}_L,\boldsymbol{U}_R)$ denotes the numerical viscosity and is assumed to be not lesser than $\max_{1\leqslant m\leqslant 8,\boldsymbol{U}}\{|\lambda_{n^i}^m|\}$ in order to preserve the stability, and $\lambda_{n^i}^m$ denotes the mth eigenvalue of the Jacobian matrix of $\boldsymbol{F}_{n^i}$ with respect to $\boldsymbol{U}$. Here, we have assumed that

$$\boldsymbol{U}_L = \boldsymbol{U}_{A_{j+\frac{1}{2},k+\frac{1}{2}}}(\boldsymbol{x}^i,t), \quad \boldsymbol{U}_R = \boldsymbol{U}_{A^i_{j+\frac{1}{2},k+\frac{1}{2}}}(\boldsymbol{x}^i,t),$$

where $\boldsymbol{x}^i$ and $A^i_{j+\frac{1}{2},k+\frac{1}{2}}$ denote the centroid coordinates of the edge L^i and the ith neighbor of the control volume $A_{j+\frac{1}{2},k+\frac{1}{2}}$, respectively.

System (2.9) may be approximated by any stable time discretization. For example, we use an explicit second-order accurate TVD Runge–Kutta method [42] to evolve solutions of ideal MHD equations from t_n to t_{n+1}:

$$\boldsymbol{U}^* = \boldsymbol{U}^n + \Delta t L(\boldsymbol{U}^n), \tag{2.11}$$

$$\boldsymbol{U}^{n+1} = \frac{1}{2}(\boldsymbol{U}^n + \boldsymbol{U}^* + \Delta t L(\boldsymbol{U}^*)), \tag{2.12}$$

where $L(\boldsymbol{U})$ denotes the term at the right hand side of (2.9).

2.2. A staggered constrained transport method

Assuming the conservative variables $\boldsymbol{U}^{n+1}$ have been computed by using the base scheme (2.9)–(2.12), then we evolve the magnetic potential $\mathscr{A}$ at each corner $\boldsymbol{x}_{j,k}$ by a second-order accurate approximation of (2.3), same as one in [52],

$$\mathscr{A}_{j,k}^{n+1} = \mathscr{A}_{j,k}^n - \Delta t \Omega_{j,k}^{n+1/2}, \tag{2.13}$$

where

$$\Omega_{j,k}^{n+1/2} = \tfrac{1}{8}\left(\Omega^n_{j-\frac{1}{2},k-\frac{1}{2}} + \Omega^n_{j+\frac{1}{2},k-\frac{1}{2}} + \Omega^n_{j-\frac{1}{2},k+\frac{1}{2}} + \Omega^n_{j+\frac{1}{2},k+\frac{1}{2}}\Omega^{\bigstar}_{j-\frac{1}{2},k-\frac{1}{2}} + \Omega^{\bigstar}_{j+\frac{1}{2},k-\frac{1}{2}} + \Omega^{\bigstar}_{j-\frac{1}{2},k+\frac{1}{2}} + \Omega^{\bigstar}_{j+\frac{1}{2},k+\frac{1}{2}}\right).$$

Here $\Omega^n = -u_1^n B_2^n + u_2^n B_1^n$ and $\Omega^{\bigstar} = -u_1^{n+1}B_2^{n+1} + u_2^{n+1}B_1^{n+1}$. Then, we compute a new magnetic field $\boldsymbol{B}_{A_{j+\frac{1}{2},k+\frac{1}{2}}}(\boldsymbol{x},t_{n+1})$ which is divergence-free in $A_{j+\frac{1}{2},k+\frac{1}{2}}$ at $t = t_{n+1}$ according to the known magnetic potential $\mathscr{A}^{n+1}$ in the following way.

In the control volume $A_{j+\frac{1}{2},k+\frac{1}{2}}$, we reconstruct locally the magnetic potential as follows:

$$\mathscr{A}_{j+\frac{1}{2},k+\frac{1}{2}}(\boldsymbol{x},t_{n+1}) = \alpha^0 + \alpha^1 x_1 + \alpha^2 x_2 + \alpha^3 x_1 x_2 + \alpha^4 x_1^2 + \alpha^5 x_2^2, \tag{2.14}$$

where six coefficients α^i, $i = 0,\ldots,5$, are determined uniquely by

$$\mathscr{A}_{j+\frac{1}{2},k+\frac{1}{2}}(\boldsymbol{x}_{j+p,k+q},t_{n+1}) = \mathscr{A}^{n+1}_{j+p,k+q}, \quad p,q = 0,1,$$

and

$$\left(\frac{\partial B_1}{\partial x_2}\right)_{j+\frac{1}{2},k+\frac{1}{2}} = 2\alpha^5, \quad \left(\frac{\partial B_2}{\partial x_1}\right)_{j+\frac{1}{2},k+\frac{1}{2}} = -2\alpha^4.$$

Here $\left(\frac{\partial B_1}{\partial x_2}\right)_{j+\frac{1}{2},k+\frac{1}{2}}$ and $(\frac{\partial B_2}{\partial x_1})_{j+\frac{1}{2},k+\frac{1}{2}}$ are corresponding limited slopes of the magnetic field according to cell averages of the magnetic field calculated by the base scheme or cell-vertex values of the magnetic potential, see (2.15) and (2.16). After computing α^i in (2.14), we may get a divergence-free magnetic field $\boldsymbol{B}_{A_{j+\frac{1}{2},k+\frac{1}{2}}}(\boldsymbol{x}, t_{n+1})$ as well as $\boldsymbol{B}_L$ and $\boldsymbol{B}_R$ in the numerical flux (2.10).

The cell averages of the magnetic field $\boldsymbol{B}_{j+\frac{1}{2},k+\frac{1}{2}}$ may also be calculated by a finite volume interpretation from cell-vertex values of the magnetic potential. Since $B_1 = \partial\mathscr{A}/\partial x_2$, integrating over the control volume $A_{j+\frac{1}{2},k+\frac{1}{2}}$ gives

$$\begin{aligned}(B_1)_{j+\frac{1}{2},k+\frac{1}{2}} &= \frac{1}{|A_{j+\frac{1}{2},k+\frac{1}{2}}|}\int_{A_{j+\frac{1}{2},k+\frac{1}{2}}} B_1\,\mathrm{d}\boldsymbol{x}\\ &= \frac{1}{|A_{j+\frac{1}{2},k+\frac{1}{2}}|}\int_{A_{j+\frac{1}{2},k+\frac{1}{2}}} \frac{\partial\mathscr{A}}{\partial x_2}\,\mathrm{d}\boldsymbol{x} = \frac{1}{|A_{j+\frac{1}{2},k+\frac{1}{2}}|}\sum_{i=1}^{4}\int_{L^i}\mathscr{A}n_2^i\,\mathrm{d}l\\ &\doteq -\frac{1}{2|A_{j+\frac{1}{2},k+\frac{1}{2}}|}[(\mathscr{A}_{j,k}+\mathscr{A}_{j+1,k})(x_{j+1,k}-x_{j,k}) + (\mathscr{A}_{j+1,k}+\mathscr{A}_{j+1,k+1})(x_{j+1,k+1}-x_{j+1,k})\\ &\quad + (\mathscr{A}_{j+1,k+1}+\mathscr{A}_{j,k+1})(x_{j,k+1}-x_{j+1,k+1}) + (\mathscr{A}_{j,k+1}+\mathscr{A}_{j,k})(x_{j,k}-x_{j,k+1})].\end{aligned} \tag{2.15}$$

Similarly, the x_2-component of the cell averaged magnetic field can be obtained through the integration of B_2 over the control volume

$$\begin{aligned}(B_2)_{j+\frac{1}{2},k+\frac{1}{2}} &= -\frac{1}{2|A_{j+\frac{1}{2},k+\frac{1}{2}}|}[(\mathscr{A}_{j,k}+\mathscr{A}_{j+1,k})(y_{j+1,k}-y_{j,k}) + (\mathscr{A}_{j+1,k}+\mathscr{A}_{j+1,k+1})(y_{j+1,k+1}-y_{j+1,k})\\ &\quad + (\mathscr{A}_{j+1,k+1}+\mathscr{A}_{j,k+1})(y_{j,k+1}-y_{j+1,k+1}) + (\mathscr{A}_{j,k+1}+\mathscr{A}_{j,k})(y_{j,k}-y_{j,k+1})].\end{aligned} \tag{2.16}$$

If the mesh is rectangular, above expressions are equivalent to the CT method proposed in [22], in which the cell-centered magnetic field is obtained through a simple linear interpolation:

$$\begin{aligned}[B_1]_{j+\frac{1}{2},k+\frac{1}{2}} &= \frac{1}{2}\left([b_1]_{j,k+\frac{1}{2}} + [b_1]_{j+1,k+\frac{1}{2}}\right),\\ [B_2]_{j+\frac{1}{2},k+\frac{1}{2}} &= \frac{1}{2}\left([b_2]_{j+\frac{1}{2},k} + [b_2]_{j+\frac{1}{2},k+1}\right),\end{aligned}$$

where the edge-based magnetic field is defined by

$$[b_1]_{j,k+\frac{1}{2}} = \frac{1}{\Delta x_2}(\mathscr{A}_{j,k+1}-\mathscr{A}_{j,k}),\quad [b_2]_{j+\frac{1}{2},k} = -\frac{1}{\Delta x_1}(\mathscr{A}_{j+1,k}-\mathscr{A}_{j,k}).$$

It is easy validate that the magnetic field is divergence-free in the sense of

$$\begin{aligned}0 &= \frac{1}{2\Delta x_1}\left([B_1]_{j+\frac{1}{2},k-\frac{1}{2}} + [B_1]_{j+\frac{1}{2},k+\frac{1}{2}} - [B_1]_{j-\frac{1}{2},k-\frac{1}{2}} - [B_1]_{j-\frac{1}{2},k+\frac{1}{2}}\right)\\ &\quad + \frac{1}{2\Delta x_2}\left([B_2]_{j-\frac{1}{2},k+\frac{1}{2}} + [B_2]_{j+\frac{1}{2},k+\frac{1}{2}} - [B_2]_{j-\frac{1}{2},k-\frac{1}{2}} - [B_2]_{j+\frac{1}{2},k-\frac{1}{2}}\right).\end{aligned}$$

3. An adaptive moving mesh method

3.1. Mesh-redistribution

In the variational approach, the mesh map between the domains Ω_c and Ω_p is usually provided by minimizing a functional of the following form:

$$E[\boldsymbol{\xi}] = \frac{1}{2}\sum_{i=1}^{2}\int_{\Omega_p}\nabla_{\boldsymbol{x}}^{\mathrm{T}}\xi_i G_i^{-1}\nabla_{\boldsymbol{x}}\xi_i\,\mathrm{d}\boldsymbol{x}, \tag{3.1}$$

where $\boldsymbol{\xi} = (\xi_1, \xi_2)$ denotes coordinates in the logical domain Ω_c, $\nabla_{\boldsymbol{x}} = (\partial_{x_1}, \partial_{x_2})^{\mathrm{T}}$, G_i are given symmetric positive definite matrices called *monitor functions*, depending on the underlying solution to be adapted. More terms can be added to the functional (3.1) to control other aspects of the mesh such as orthogonality and mesh alignment with a given vector field, see e.g. [9,11].

The simplest choice of the monitor functions is $G_i = \omega I$, $i = 1, 2$, see [56], where I denotes the identity matrix and ω is a positive weight function, e.g.

$$\omega(\boldsymbol{U}) = \sqrt{1 + \alpha_1 \left(\frac{|\nabla_{\boldsymbol{x}} \rho|}{\max \rho}\right)^2 + \alpha_2 \left(\frac{|\nabla_{\boldsymbol{x}} p|}{\max p}\right)^2 + \alpha_3 \left(\frac{|\nabla_{\boldsymbol{x}} p_{\mathrm{mag}}|}{\max p_{\mathrm{mag}}}\right)^2} \tag{3.2}$$

for the MHD equations (1.1)–(1.4). Using this choice, we deduce the Euler–Lagrange equations of the functional (3.1) to

$$\nabla_{\boldsymbol{x}} \cdot \left(\frac{1}{\omega} \nabla_{\boldsymbol{x}} \xi_i\right) = 0, \quad i = 1, 2. \tag{3.3}$$

Solving (3.3) gives a map from Ω_p to Ω_c. Typically, the map transforms a uniform mesh in Ω_c to cluster grid points in the regions of Ω_p where the solution has large gradients.

In practice, Ω_p may have a very complex geometry, and as a result it is not realistic to solve (3.3) directly. Therefore we usually solve the corresponding mesh generation equations on Ω_c by interchanging the dependent and independent variables in (3.3). Doing so, the resulting system on Ω_c is more complicated and requires more computational effort. An alternative approach is to consider a functional [14,47]:

$$\widetilde{E}[\boldsymbol{x}] = \frac{1}{2} \sum_{i=1}^{2} \int_{\Omega_c} \nabla_{\boldsymbol{\xi}}^{\mathrm{T}} x_i G_i \nabla_{\boldsymbol{\xi}} x_i \, \mathrm{d}\boldsymbol{\xi} \tag{3.4}$$

where $\nabla_{\boldsymbol{\xi}} = (\partial_{\xi_1}, \partial_{\xi_2})^{\mathrm{T}}$.

The corresponding Euler–Lagrange equations with the choice $G_i = \omega I$, $i = 1, 2$, are

$$\nabla_{\boldsymbol{\xi}} \cdot (\omega \nabla_{\boldsymbol{\xi}} x_i) = 0, \quad i = 1, 2. \tag{3.5}$$

In our computations, we will use the Gauss–Seidel type iteration method [47] to solve the mesh-moving Eq. (3.3) or (3.5). For example, the iteration method for (3.5) is written as follows:

$$\alpha_{j+\frac{1}{2},k}\left(\boldsymbol{x}_{j+1,k}^{[v]} - \boldsymbol{x}_{j,k}^{[v+1]}\right) - \alpha_{j-\frac{1}{2},k}\left(\boldsymbol{x}_{j,k}^{[v+1]} - \boldsymbol{x}_{j-1,k}^{[v+1]}\right) + \beta_{j,k+\frac{1}{2}}\left(\boldsymbol{x}_{j,k+1}^{[v]} - \boldsymbol{x}_{j,k}^{[v+1]}\right) - \beta_{j,k-\frac{1}{2}}\left(\boldsymbol{x}_{j,k}^{[v+1]} - \boldsymbol{x}_{j,k-1}^{[v+1]}\right) = 0 \tag{3.6}$$

for $1 \leqslant j \leqslant N_{\xi_1}$ and $1 \leqslant k \leqslant N_{\xi_2}$, $v = 0, 1, \ldots$, where

$$\alpha_{j\pm\frac{1}{2},k} = \omega\left(\boldsymbol{U}_{j\pm\frac{1}{2},k}^{[v]}\right) = \frac{1}{2}\left(\omega\left(\boldsymbol{U}_{j\pm\frac{1}{2},k+\frac{1}{2}}^{[v]}\right) + \omega\left(\boldsymbol{U}_{j\pm\frac{1}{2},k-\frac{1}{2}}^{[v]}\right)\right),$$

$$\beta_{j,k\pm\frac{1}{2}} = \omega\left(\boldsymbol{U}_{j,k\pm\frac{1}{2}}^{[v]}\right) = \frac{1}{2}\left(\omega\left(\boldsymbol{U}_{j+\frac{1}{2},k\pm\frac{1}{2}}^{[v]}\right) + \omega\left(\boldsymbol{U}_{j-\frac{1}{2},k\pm\frac{1}{2}}^{[v]}\right)\right).$$

Remark 3.1. In practice it is common to use some temporal or spatial *smoothing* on the monitor function to obtain smoother meshes, and avoid very singular mesh and/or large approximation error around the stiff solution areas. In this work, we apply the following low pass filter to smooth the monitor [47]:

$$\begin{aligned}\omega_{j+\frac{1}{2},k+\frac{1}{2}} \leftarrow{}& \frac{1}{4}\omega_{j+\frac{1}{2},k+\frac{1}{2}} + \frac{1}{8}\left(\omega_{j+\frac{3}{2},k+\frac{1}{2}} + \omega_{j+\frac{1}{2},k+\frac{3}{2}} + \omega_{j-\frac{1}{2},k+\frac{1}{2}} + \omega_{j+\frac{1}{2},k-\frac{1}{2}}\right) \\ &+ \frac{1}{16}\left(\omega_{j+\frac{3}{2},k+\frac{3}{2}} + \omega_{j+\frac{3}{2},k-\frac{1}{2}} + \omega_{j-\frac{1}{2},k+\frac{3}{2}} + \omega_{j-\frac{1}{2},k-\frac{1}{2}}\right),\end{aligned}$$

where $\omega_{j+\frac{1}{2},k+\frac{1}{2}} = \omega(\boldsymbol{U}_{j+\frac{1}{2},k+\frac{1}{2}})$.

Remark 3.2. The iteration number in (3.6) is generally controlled by a finite integer number, denoted by μ, $0 < \mu \leqslant 5$. The iteration (3.6) guarantees essentially that the new grid point $\boldsymbol{x}_{j,k}^{[v+1]}$ always lies in one of four cells neighboring the old grid point $\boldsymbol{x}_{j,k}^{[v]}$.

3.2. Interpolation of the conservation variables

For convenience, we use $\{\widetilde{\boldsymbol{x}}_{j,k}\}$ and $\{\boldsymbol{x}_{j,k}\}$ to denote the new and old meshes in this and next subsections, i.e., $\widetilde{\boldsymbol{x}}_{j,k} := \boldsymbol{x}_{j,k}^{[v+1]}$, and $\boldsymbol{x}_{j,k} := \boldsymbol{x}_{j,k}^{[v]}$, $v \geqslant 0$. After obtaining the new mesh, we need to compute cell averages of the conservative variables over $\widetilde{A}_{j+\frac{1}{2},k+\frac{1}{2}}$. Tang and Tang [47] advised a simple re-mapping method that can preserve conservation of the variable $\boldsymbol{U}$ in the following sense:

$$\sum_{j,k} |\widetilde{A}_{j+\frac{1}{2},k+\frac{1}{2}}| \widetilde{\boldsymbol{U}}_{j+\frac{1}{2},k+\frac{1}{2}} = \sum_{j,k} |A_{j+\frac{1}{2},k+\frac{1}{2}}| \boldsymbol{U}_{j+\frac{1}{2},k+\frac{1}{2}}. \tag{3.7}$$

Here we give a simplified geometrical approach to calculate new cell averages $\widetilde{\boldsymbol{U}}_{j+\frac{1}{2},k+\frac{1}{2}}$ which also satisfies (3.7).

As shown in Fig. 2, cell averages of the conservative variables over the quadrangle $\widetilde{A}_{j+\frac{1}{2},k+\frac{1}{2}}$ may be computed as

$$|\widetilde{A}_{j+\frac{1}{2},k+\frac{1}{2}}| \widetilde{\boldsymbol{U}}_{j+\frac{1}{2},k+\frac{1}{2}} = |A_{j+\frac{1}{2},k+\frac{1}{2}}| \boldsymbol{U}_{j+\frac{1}{2},k+\frac{1}{2}} + \sum_{i=1}^{4} \widehat{\boldsymbol{F}}_i, \tag{3.8}$$

where $\widehat{\boldsymbol{F}}_i$ denotes the integration of $\boldsymbol{U}$ over the domain D_i, $i = 1,\ldots,4$. Here we have omitted the subscripts j and k of $\widehat{\boldsymbol{F}}_i$ and D_i for simplicity. Since only cell averages of $\boldsymbol{U}$ over $A_{j+\frac{1}{2},k+\frac{1}{2}}$ is known, we should give an approximation of $\widehat{\boldsymbol{F}}_i$ instead of its exact value. As an example, we consider the case of $i = 1$, and compute

$$|D_1| := \frac{1}{2}((\widetilde{x}_{j+1,k+1} - x_{j+1,k})(y_{j+1,k+1} - \widetilde{y}_{j+1,k}) - (\widetilde{y}_{j+1,k+1} - y_{j+1,k})(x_{j+1,k+1} - \widetilde{x}_{j+1,k})). \tag{3.9}$$

Obviously, $|D_1|$ is the area of D_1, which is positive if $\boldsymbol{x}_{j+1,k}$, $\widetilde{\boldsymbol{x}}_{j+1,k}$, $\widetilde{\boldsymbol{x}}_{j+1,k+1}$ and $\boldsymbol{x}_{j+1,k+1}$ are located in a counter-clockwise order; otherwise it is negative if those four points are located in a clockwise order. For first order interpolation, $\widehat{\boldsymbol{F}}_1$ has the form of

$$\widehat{\boldsymbol{F}}_1 = \begin{cases} |D_1| \boldsymbol{U}_{j+\frac{3}{2},k+\frac{1}{2}}, & \text{if } |D_1| > 0, \\ |D_1| \boldsymbol{U}_{j+\frac{1}{2},k+\frac{1}{2}}, & \text{if } |D_1| \leqslant 0. \end{cases} \tag{3.10}$$

For a high order accurate interpolation, the initial reconstruction is required to get $\boldsymbol{U}_L$ and $\boldsymbol{U}_R$ along cell boundaries instead of $\boldsymbol{U}_{j+\frac{3}{2},k+\frac{1}{2}}$ and $\boldsymbol{U}_{j+\frac{1}{2},k+\frac{1}{2}}$. We refer the readers to Section 2.1 for a detailed description of the initial reconstruction.

Since two neighboring quadrangles share the same flux $\widehat{\boldsymbol{F}}_i$ but with opposite signs, the interpolation (3.8) satisfies (3.7).

Remark 3.3. In our MHD computations, we only interpolate the fluid variables, such as the mass, momentum, and total energy by using the above interpolation procedure. The magnetic field is "remapped" to the new mesh through the interpolation of the magnetic potential, which will be given in the coming Section 3.3.

3.3. Interpolation of the magnetic potential

In this subsection, we begin to update the magnetic potential $\mathscr{A}$ as well as the magnetic field $\boldsymbol{B}$ on the resulting new mesh $\{\widetilde{\boldsymbol{x}}_{j,k}\}$ according to the information on the old mesh $\{\boldsymbol{x}_{j,k}\}$. Since the magnetic potential $\mathscr{A}$ is a

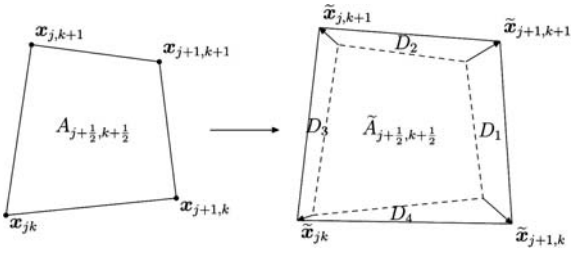

Fig. 2. The control volume before and after mesh-moving.

non-conservative variable and approximated at cell vertices, it is unnecessary to remap $\mathscr{A}$ conservatively. However, interpolation of the magnetic potential does play an important role in the moving mesh method. Unexpected results can occur for some problems if it is done inappropriately.

In the staggered CT method, we may use a traditional interpolation on the cell in which the new grid point lies. For example, a bilinear interpolation can be used by solving a 3×3 linear system. However, this approach may introduce large dissipation at each iteration step. Another approach is to use a high-resolution Hamilton–Jacobi type interpolation derived from Taylor's expansion and a high-resolution approximation of the following equation

$$\widetilde{\mathscr{A}}_{j,k} = \mathscr{A}_{j,k} + (\nabla_{\boldsymbol{x}}\mathscr{A})_{j,k} \cdot (\widetilde{\boldsymbol{x}}_{j,k} - \boldsymbol{x}_{j,k}). \tag{3.11}$$

We refer the readers to [48] for the detailed implementation. Moreover, it is possible to replace (3.11) by

$$\widetilde{\mathscr{A}}_{j,k} = \mathscr{A}_{j,k} - (B_2)_{j,k}(\widetilde{x} - x)_{j,k} + (B_1)_{j,k}(\widetilde{y} - y)_{j,k}. \tag{3.12}$$

After that, we may compute a piecewise linear, divergence-free, magnetic field $\widetilde{\boldsymbol{B}}$ on the new mesh $\{\widetilde{\boldsymbol{x}}_{j,k}\}$ following the approach given in Section 2.2. It is easy to show that conservation of B_1 and B_2 can be preserved, when (3.11) is adopted.

Remark 3.4. It should be noted that there are two similar works on reconstruction or interpolation of the divergence-free magnetic field. Balsara [5] used a quadratic polynomial to directly reconstruct a divergence-free magnetic field B. Bochev and Shashkov [8] also used the potential field to give the divergence-free magnetics. Their remapping algorithm is based on a local optimization and finite element discretization so that it is a bit complicated actually even though their algorithm has some other advantages. Moreover, they did not consider combination of the remapping phase with evolution of the governing equations there.

4. Solution procedure

Our solution procedure consists of two independent parts: MHD evolution and iterative mesh-redistribution. The first part is a divergence-free finite volume method with high-resolution, see Section 2. In each iteration of the second part, mesh points are first redistributed by the Gauss–Seidel method, e.g. (3.6), and then $(\rho, \rho\boldsymbol{u}, E)$ is updated on the resulting new meshes by the conservative-interpolation formula (3.8), while the magnetic potential $\mathscr{A}$ is remapped by the non-conservative approach, see Section 3.3. The algorithm ensures that the reconstructed magnetic field is divergence-free in each control volume $A_{j+\frac{1}{2},k+\frac{1}{2}}$.

The solution procedure can be illustrated by the following flowchart:

Algorithm AM^3-2DMHD

Step 1: If the time level $n = 0$, give an initial partition $\{\boldsymbol{x}^{[0]}_{j,k}\}$ of the physical domain Ω_p and a uniform partition of the logical domain Ω_c; compute cell average of the conservative variables $\boldsymbol{U}^{[0]}_{j+\frac{1}{2},k+\frac{1}{2}}$ based on the initial data and the initial magnetic potential $\mathscr{A}^{[0]}_{j,k}$.
Else if $n > 0$, set $\boldsymbol{x}^{[0]}_{j,k} := \boldsymbol{x}^{n}_{j,k}$, $\boldsymbol{U}^{[0]}_{j+\frac{1}{2},k+\frac{1}{2}} := \boldsymbol{U}^{n}_{j+\frac{1}{2},k+\frac{1}{2}}$, and $\mathscr{A}^{[0]}_{j,k} := \mathscr{A}^{n}_{j,k}$.

Step 2: For $v = 0, 1, 2, \ldots, \mu - 1$, do the following:

(1) Compute and smoothen the monitor function $\omega^{[v]}_{j+\frac{1}{2},k+\frac{1}{2}}$, and move the mesh point $\boldsymbol{x}^{[v]}_{j,k}$ to a new position $\boldsymbol{x}^{[v+1]}_{j,k}$ based on the Gauss–Seidel iteration method described in Section 3.1.

(2) Update the conservative variables (without including the magnetic field) on the resulting new mesh $\{\boldsymbol{x}^{[v+1]}_{j,k}\}$, i.e. compute $\boldsymbol{U}^{[v+1]}_{j+\frac{1}{2},k+\frac{1}{2}}$, with the interpolation formula described in Section 3.2.

(3) Update the magnetic potential and the magnetic field on the new mesh $\{\boldsymbol{x}^{[v+1]}_{j,k}\}$, i.e. compute $\mathscr{A}^{[v+1]}$ and $\boldsymbol{B}^{[v+1]}$, with the approach described in Section 3.3.

Step 3: After redistributing the grid points, the initial state variables on the new mesh $\{\boldsymbol{x}^{n+1}_{j,k}\}$ with $\boldsymbol{x}^{n+1}_{j,k} := \boldsymbol{x}^{[\mu]}_{j,k}$ are re-set as $\boldsymbol{U}^{n}_{j+\frac{1}{2},k+\frac{1}{2}} := \boldsymbol{U}^{[\mu]}_{j+\frac{1}{2},k+\frac{1}{2}}$ and $\mathscr{A}^{n}_{j,k} := \mathscr{A}^{[\mu]}_{j,k}$. Then, solve the MHD equations as follows:

(1) Determine the time step size Δt_n according to the CFL condition.
(2) Solve the MHD equations with a second-order accurate divergence-free scheme to get ρ^{n+1}, $\rho\boldsymbol{u}^{n+1}$, E^{n+1}, and $\boldsymbol{B}^{n+1}$.
(3) Compute the electric field $\Omega_{j,k}^{n+1/2}$ according to $\boldsymbol{u}^p$ and $\boldsymbol{B}^p$, $p = n$ and $n+1$.
(4) Update the magnetic potential with $A_{j,k}^{n+1} = A_{j,k}^n - \Delta t \Omega_{j,k}^{n+1/2}$, and reconstruct it to give the divergence-free magnetic field $\boldsymbol{B}_{A_{j+\frac{1}{2},k+\frac{1}{2}}}(\boldsymbol{x}, t_{n+1})$ for the next time step.

Step 4: If $t \geqslant T$, then do step 2, save the result and stop. Otherwise, go to step 1 for the next time circle.

Before ending this section, we give a few remarks on the above algorithm here.

Remark 4.1. If the initial magnetic potential cannot be expressed by an analytical form, we compute the magnetic potential $\mathscr{A}$ at $t = 0$ by solving a Poisson equation of the form [38]:

$$\nabla^2 \mathscr{A} = -\nabla \times \boldsymbol{B}, \tag{4.1}$$

and then use this magnetic potential $\mathscr{A}(\boldsymbol{x}, 0)$ to give the divergence-free magnetic field $\boldsymbol{B}(\boldsymbol{x}, 0)$ as initial data in numerical computations.

Remark 4.2. There are some variants to compute the electric field $\Omega_{j,k}^{n+1/2}$. For example, the spatial and temporal interpolation is first used to obtain the magnetic field

$$\boldsymbol{B}_{j,k}^{n+1/2} = \frac{1}{8}\left(\boldsymbol{B}_{j-\frac{1}{2},k-\frac{1}{2}}^n + \boldsymbol{B}_{j+\frac{1}{2},k-\frac{1}{2}}^n + \boldsymbol{B}_{j-\frac{1}{2},k+\frac{1}{2}}^n + \boldsymbol{B}_{j+\frac{1}{2},k+\frac{1}{2}}^n + \boldsymbol{B}_{j-\frac{1}{2},k-\frac{1}{2}}^{n+1} + \boldsymbol{B}_{j+\frac{1}{2},k-\frac{1}{2}}^{n+1} + \boldsymbol{B}_{j-\frac{1}{2},k+\frac{1}{2}}^{n+1} + \boldsymbol{B}_{j+\frac{1}{2},k+\frac{1}{2}}^{n+1}\right), \tag{4.2}$$

and the velocity field $\boldsymbol{u}_{j,k}^{n+1/2}$ (using the same interpolation) at cell corners. Then the electric field is computed by

$$\boldsymbol{\Omega}_{j,k}^{n+1/2} = \boldsymbol{B}_{j,k}^{n+1/2} \times \boldsymbol{u}_{j,k}^{n+1/2}. \tag{4.3}$$

Remark 4.3. The initial reconstructions may be implemented in the logical domain instead of the physical domain, because the logical domain is better in representation of the solutions than the physical domain. Furthermore, operations on the logical domain with a regular mesh grid are much easier to be performed than on the physical domain with a non-regular mesh, see Section 2.1.

Remark 4.4. In many flow situations, discontinuities may initially exist on boundaries or move to boundaries at a later time. As a consequence, redistribution of boundary points should be made in order to improve the quality of the solution near boundary. The redistribution strategy given in [47] may be used to move the boundary points in order to improve the solution resolution.

5. Numerical tests

In this section, the moving mesh algorithm, AM^3-2DMHD, described above is applied to several ideal MHD problems, which are the smooth Alfvén wave problem, 2D and 2.5D shock tube problems, two rotor problems, the stringent blast problem, and the cloud–shock interaction problem. The first problem is given to validate accuracy of the proposed method due to smooth solutions. Other examples are given to check numerical resolution and efficiency in keeping the magnetic field divergence-free and resolving strong shock wave etc. In our computations, we adopt the local Lax-Friedrichs flux, i.e. the flux (2.10) with $\boldsymbol{Q}^i = \max_{1\leqslant m\leqslant 8}\{|\lambda_{n^i}^m(\boldsymbol{U}_L)|, |\lambda_{n^i}^m(\boldsymbol{U}_R)|\}$ for the base scheme due to its simplicity, and van Leer's limiter [54] for approximate slopes, and take the CFL number as 0.5, the maximum iteration number $\mu = 5$, and the monitor function (3.2) with $\alpha_1 = \alpha_2 = \alpha_3 = 1$, unless otherwise stated.

5.1. Smooth Alfvén wave problem

First we solve the smooth Alfvén problem [52] to check accuracy of the algorithm AM^3-2DMHD. This problem describes propagation of a circularly polarized Alfvén wave in the domain $\Omega_p = [0, 2/\sqrt{3}] \times [0, 2]$ at an angle of 30° relative to the x-axis. The initial conditions are taken as

$$\rho = 1, \quad u_\parallel = 0, \quad u_\perp = 0.1\sin(2\pi\zeta), \quad u_3 = 0.1\cos(2\pi\zeta),$$
$$p = 0.1, \quad B_\parallel = 1, \quad B_\perp = u_\perp, \quad B_3 = u_3,$$

with $\gamma = 5/3$, where $\zeta = x_1\cos\alpha + x_2\sin\alpha$. In this problem, the Alfvén wave propagates periodically towards the origin with a constant speed $B_\parallel/\sqrt{\rho} = 1$ and returns to its initial state whenever t becomes an integer.

The domain is assumed to be divided into $N \times 2N$. As in [52], for each value N, we estimate the relative numerical error of any fluid variable v using

$$\delta_N(v) = \frac{\sum_{j=1}^{N}\sum_{k=1}^{2N}|v_{j,k}^N - v_{j,k}^{\text{exact}}|}{\sum_{j=1}^{N}\sum_{k=1}^{2N}|v_{j,k}^{\text{exact}}|},$$

and the convergence rate by

$$R_N = \log_2(\delta_{N/2}/\delta_N),$$

where δ_N is an average and given as

$$\delta_N = \frac{1}{4}(\delta_N(u_\perp) + \delta_N(u_3) + \delta_N(B_\perp) + \delta_N(B_3)).$$

Table 1 gives the relative numerical errors and convergence rates at $t = 2$ and 10. Because the density and pressure are almost constant, the mesh points is moved slightly. We may obtain the second order accuracy. The results are similar to that of the fixed mesh solutions. It is worth noting that the accuracy of an adaptive moving mesh algorithm is generally dependent on choice of the monitor function $\omega(\boldsymbol{U})$. Table 2 shows computed results obtained by the present algorithm but with a different monitor function $\omega = \sqrt{1 + \alpha(|\nabla B_3|/\max|B_3|)^2}$, where $\alpha = 0$ and 0.05.

5.2. The 2D shock tube problem

The second example is to solve the quasi-2D shock tube problem subject to initial conditions

$$\boldsymbol{W} = \begin{cases} (1, -0.4, 0, 0, 1, 0.75, 1, 0), & \text{if } \zeta < 0, \\ (0.2, -0.4, 0, 0, 0.1, 0.75, -1, 0), & \text{if } \zeta > 0. \end{cases}$$

where $\boldsymbol{W} = (\rho, u_\parallel, u_\perp, u_3, p, B_\parallel, B_\perp, B_3)$ and $\zeta = x_1\cos 30^\circ + x_2\sin 30^\circ$. It is actually an extension of the 1D shock tube problem of Brio and Wu [12], who designed to show the formation of compound wave in MHDs.

In our numerical computations, we take $\gamma = 5/3$, $\alpha_1 = 2$, $\alpha_2 = 1$, $\alpha_3 = 0$, and the computational domain $\Omega_p = [-1.2, 1.2] \times [-1, 1]$ with zeroth order extrapolation boundaries at $x = \pm 1.2$ and the "shifted" period boundaries at $y = \pm 1$, that is,

$$\boldsymbol{U}(x, 1 + \tilde{y}, t) = \boldsymbol{U}(x + 2\tan 30^\circ, -1 + \tilde{y}, t),$$
$$\boldsymbol{U}(x, -1 - \tilde{y}, t) = \boldsymbol{U}(x - 2\tan 30^\circ, 1 - \tilde{y}, t),$$

where $-1.2 < x < 1.2, \tilde{y} \geqslant 0$.

Fig. 3 shows the adaptive mesh and density contours at $t = 0.3$ calculated by using the algorithm AM^3-2DMHD with 120×100 cells. We see that mesh points cluster well in the vicinities of the compound wave

Table 1
Numerical errors and convergence order for the smooth Alfvén wave problem at $t = 2$ and 10 on adaptive meshes ($\alpha_1 = \alpha_2 = 1$ and $\alpha_3 = 0$)

N	$t = 2$		$t = 10$	
	δ_N	R_N	δ_N	R_N
16	2.31e−01	–	7.71e−01	–
32	6.67e−02	1.79	2.15e−01	1.84
64	1.84e−02	1.86	6.67e−02	1.69
128	4.76e−03	1.95	1.76e−02	1.92

Table 2
Same as Table 1, except with a different monitor function $\omega = \sqrt{1 + \alpha(|\nabla B_3|/\max|B_3|)^2}$

N	Fixed mesh, $\alpha = 0$				Adaptive mesh, $\alpha = 0.05$			
	$t = 2$		$t = 10$		$t = 2$		$t = 10$	
	δ_N	R_N	δ_N	R_N	δ_N	R_N	δ_N	R_N
16	2.31e−01	–	7.71e−01	–	2.31e−01	–	7.77e−01	–
32	6.67e−02	1.79	2.15e−01	1.84	1.02e−01	1.18	2.28e−01	1.77
64	1.84e−02	1.86	6.67e−02	1.69	3.53e−02	1.53	1.08e−01	1.08
128	4.76e−03	1.95	1.76e−02	1.92	1.08e−02	1.71	3.12e−02	1.79

(an intermediate shock followed by a slow rarefaction wave), the contact discontinuity, the slow shock wave, and the left fast rarefaction wave. The right fast rarefaction wave cannot be observed from these plots, because it is very weak.

Fig. 4 gives a comparison of 1D and 2D adaptive mesh solutions to the fixed mesh solution. In Fig. 4 the 2D solution is plotted along the axis $y = 0$, and the solid line denotes the highly resolved solution of 1D MHD equations on a fixed uniform mesh of 10,000 cells for reference. Here, we have applied a linear transformation between the intervals $[-1.2, 1.2]$ and $[-1.2\cos 30°, 1.2\cos 30°]$ to the 2D solution along $y = 0$. From Fig. 4, we see that there is an excellent agreement between 1D and 2D adaptive mesh solutions; and discontinuities of the Riemann solution are sharply resolved with more clustering mesh points.

5.3. The 2.5D shock tube problem

This is another 2D Riemann problem. The initial data are given as

$$\boldsymbol{W} = \begin{cases} (1.08, 1.2, 0.01, 0.5, 0.95, 2/\sqrt{4\pi}, 3.6/\sqrt{4\pi}, 2/\sqrt{4\pi}), & \text{if } \zeta < 0, \\ (1, 0, 0, 0, 1, 2/\sqrt{4\pi}, 4/\sqrt{4\pi}, 2/\sqrt{4\pi}), & \text{if } \zeta > 0, \end{cases}$$

with $\gamma = 5/3$, where $\zeta = x_1\cos 45° + x_2\sin 45°$. It is often referred as a 2.5D shock-tube problem in the literatures, see e.g. [39,52,27], since all of the three magnetic components are non-zero. The Riemann solution for this example contains two fast shocks, two rotational discontinuities, two slow shocks, and a contact discontinuity between the two slow shocks. We take the computational domain Ω_p as $[-0.8, 0.8] \times [-0.2, 0.2]$ and divide it into 256×64 cells. Boundary conditions are specified same as those in the previous 2D Riemann problem, i.e., zeroth order extrapolation at boundaries $x = \pm 0.8$ and shifted period conditions at boundaries $y = \pm 0.2$ but with a shift of 0.4.

Fig. 5 shows the adaptive mesh and density contours at time $t = 0.2/\sqrt{2}$. Thirty equally spaced contour lines are used there. We see that fast and slow shock waves, and the contact discontinuity are resolved well,

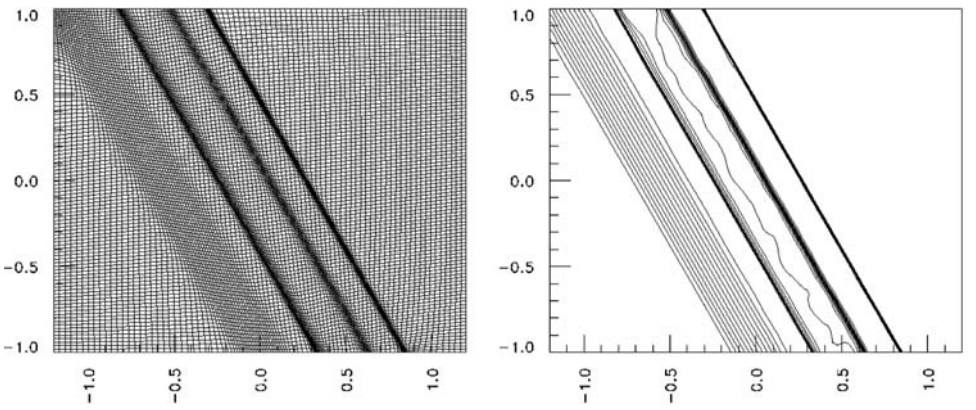

Fig. 3. 2D shock tube problem on a mesh of 120×100 cells, $t = 0.3$. Left: the adaptive mesh; right: density contours with 30 equally spaced contour lines between 0.1823 and 1.

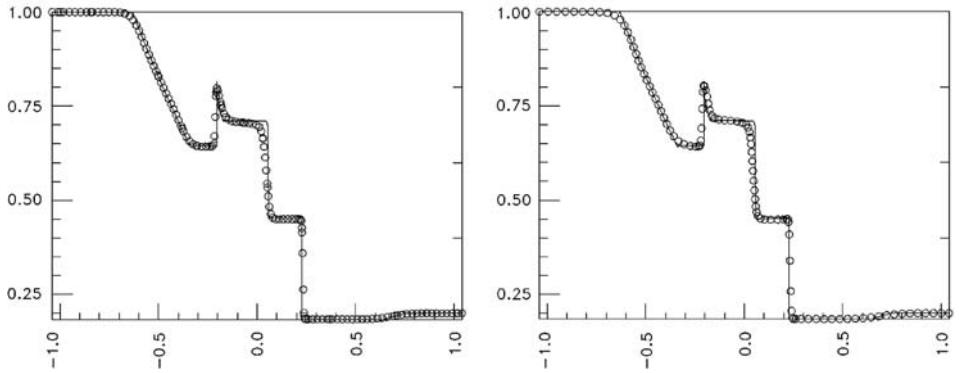

Fig. 4. Plots of the density at $t = 0.3$ for 1D and 2D shock tube problems. Left: 2D adaptive solution along the line $y = 0$; right: 1D adaptive solution with 100 points. The solid line is obtained by solving 1D MHD equations with 10,000 uniform cells.

and the mesh points cluster adaptively in the vicinities of four shocks and the contact discontinuity. In Fig. 6, we further give a comparison of 2.5D adaptive mesh solutions ('○') along $y = 0$ to 1D fixed mesh solutions with a resolution of 10,000 uniform cells (solid line). Note that we have used a linear transformation between two intervals $[-0.8, 0.8]$ and $[-0.8\cos 45°, 0.8\cos 45°]$ here. The results show that 2.5D adaptive mesh solutions are in accordance with 1D fixed mesh solutions, and several discontinuities are resolved well, even though there is a bit undershoots at one side of two slow shocks in 2D adaptive mesh solutions.

5.4. Rotor problem

This is a truly two-dimensional problem taken from [7] and has been used in [52] to compare several numerical schemes. We use exactly the same set-up of the problem as was described in [52]. The computational domain $\Omega_p = [0,1]\times[0,1]$ is divided into 200×200 cells with zeroth-order extrapolation boundary conditions for all four sides. The initial pressure and magnetic field are uniform with $B_2 = B_3 = 0$. In the middle of the domain there is a dense and rotating disk of fluid with radius $r_0 = 0.1$. Initially, in the disk, $r < r_0$, the density is $\rho = 10$, and the velocity vector $(u_1, u_2, u_3) = (-u_0(y-0.5)/r_0, u_0(x-0.5)/r_0, 0)$, where $r = \sqrt{(x-0.5)^2 + (y-0.5)^2}$. The ambient fluid is at rest with $\rho = 1$ and $\boldsymbol{u} = 0$ for $r > r_1 = 0.115$. The fluid in the cirque, $r_0 \leqslant r \leqslant r_1$, is specified by using a linear interpolation with respect to r: $\rho = 1 + 9f$, $u_1 = -fu_0(y-0.5)/r$, $u_2 = fu_0(x-0.5)/r$, where $f = (r_1 - r)/(r_1 - r_0)$ is a "taper" function, which helps to reduce initial transients. Note that the rotor is not

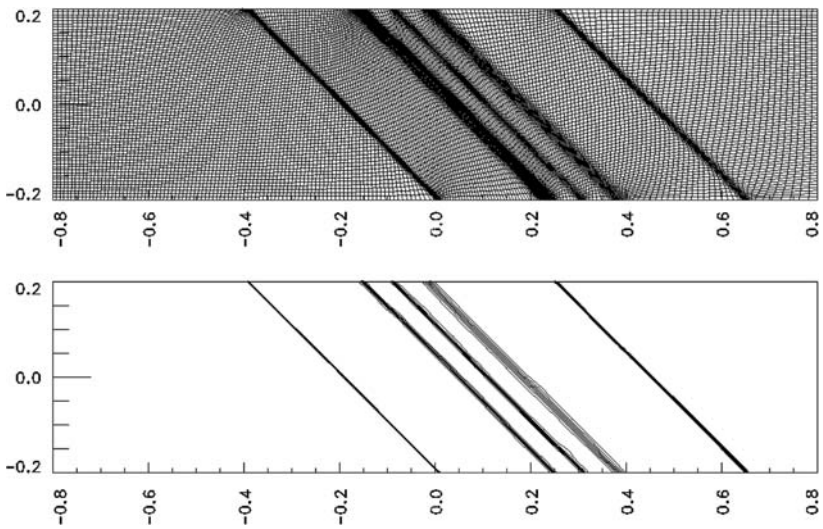

Fig. 5. 2.5D shock tube problem, $t = 0.2/\sqrt{2}$. Top: the adaptive mesh; bottom: density contours with 30 equally spaced contour lines.

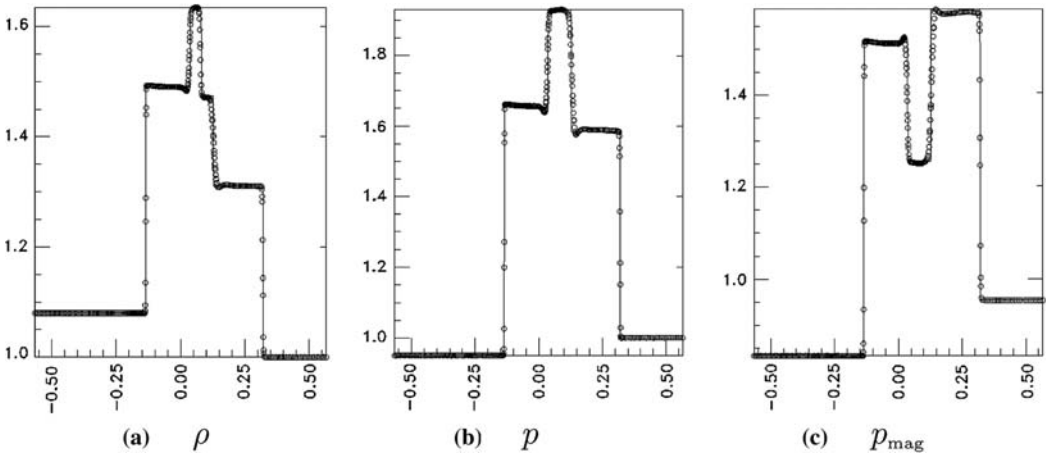

Fig. 6. A comparison of 2.5D adaptive mesh solutions ('○') along $y = 0$ to 1D fixed mesh solutions with a resolution of 10,000 uniform cells (solid line).

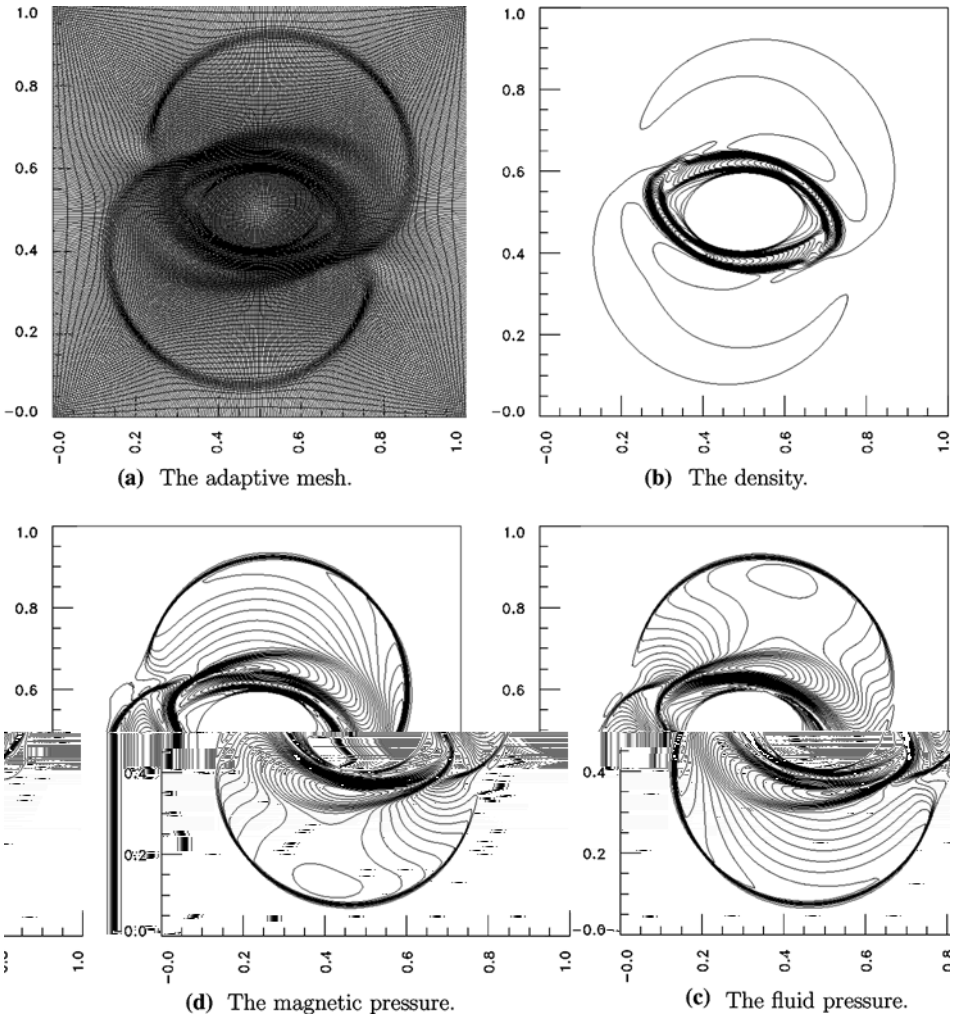

Fig. 7. Solutions of the first rotor problem at $t = 0.15$ with $N = 200$. Thirty equally spaced contour lines are used in the last three graphs.

in equilibrium due to imbalance of centrifugal forces. The magnetic field, as it winds up, will confine the rotating dense fluid into an oblate shape.

We compute two rotor problems: (i) $u_0 = 2$, $p = 1$, $B_1 = 5/\sqrt{4\pi}$, $\gamma = 1.4$, and the output time $t = 0.15$; and (ii) $u_0 = 1$, $p = 0.5$, $B_1 = 2.5/\sqrt{4\pi}$, $\gamma = 5/3$, and the output time $t = 0.295$. It was reported by Tóth [52] that many one step TVD base scheme failed to solve this problem due to negative pressure. We did not encounter any difficulties with our adaptive solver. Figs. 7 and 8 show the adaptive mesh solutions with $N = 200$ for two rotor problems, respectively, where 30 equally spaced contour lines are used for contours of the density, fluid pressure, and magnetic pressure, respectively. Figs. 9 and 10 give comparisons of the adaptive mesh solutions ('○') along the line $x = y$ to corresponding fixed mesh solutions with a resolution of 400×400 uniform cells (solid line). These results demonstrate that our adaptive mesh method is very robust, and the solutions are well resolved and also comparable with those fixed mesh solutions, including ones obtained by using the flux-CT method or the projection method, see e.g. [52].

5.5. Blast problem

Now we solve a more stringent blast problem constructed by Balsara and Spicer in [7], which involves a strong blast wave. The problem is set up on a unit square with zeroth-order extrapolation boundary condi-

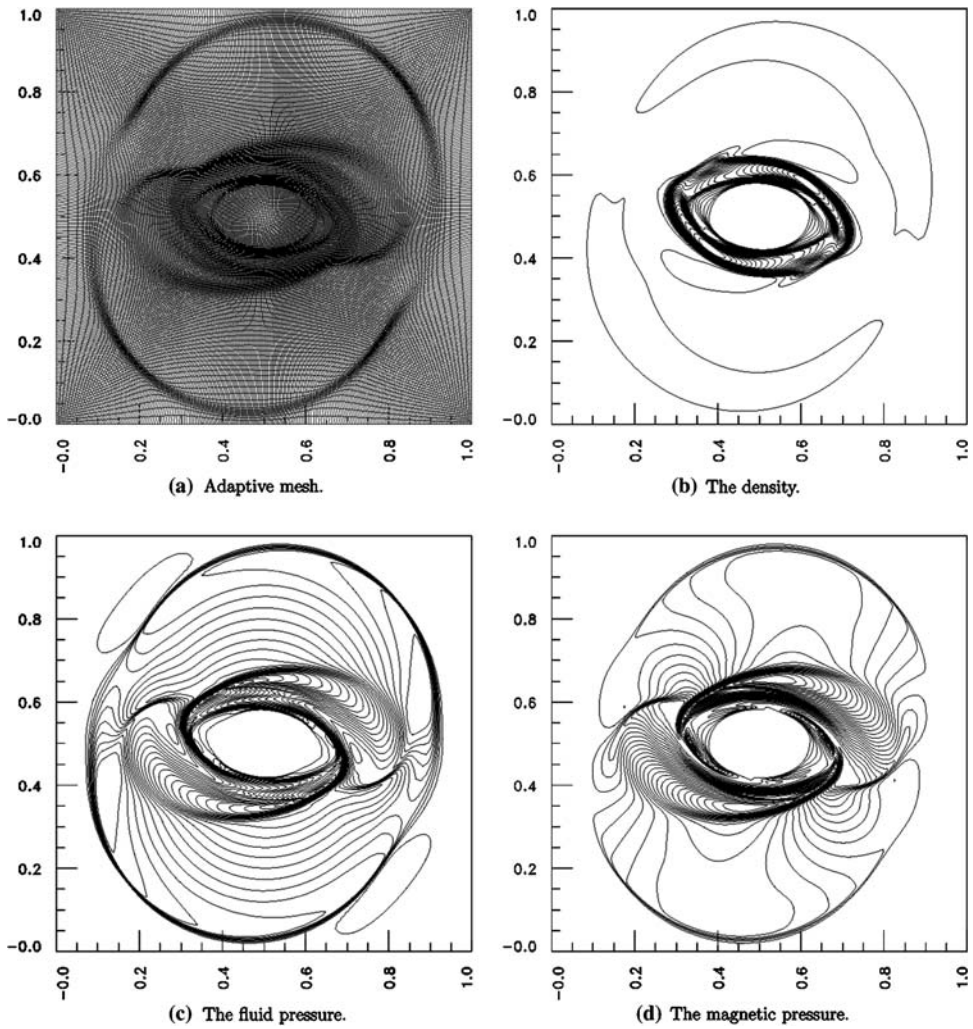

Fig. 8. Solutions to the second rotor problem at $t = 0.295$ with $N = 200$. Thirty equally spaced contour lines are used here.

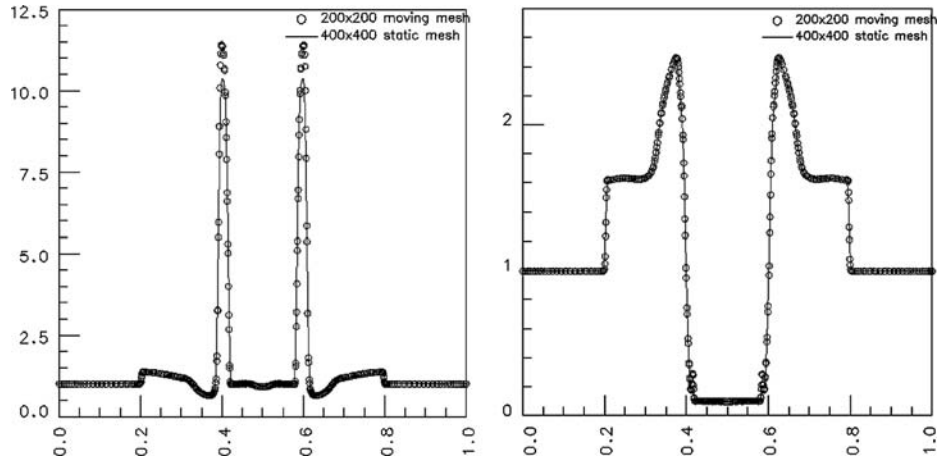

Fig. 9. A comparison of the adaptive mesh solutions ('○') of the first rotor problem to corresponding fixed mesh solutions with a resolution of 400×400 uniform cells (solid line). Left: the density; right: the magnetic pressure.

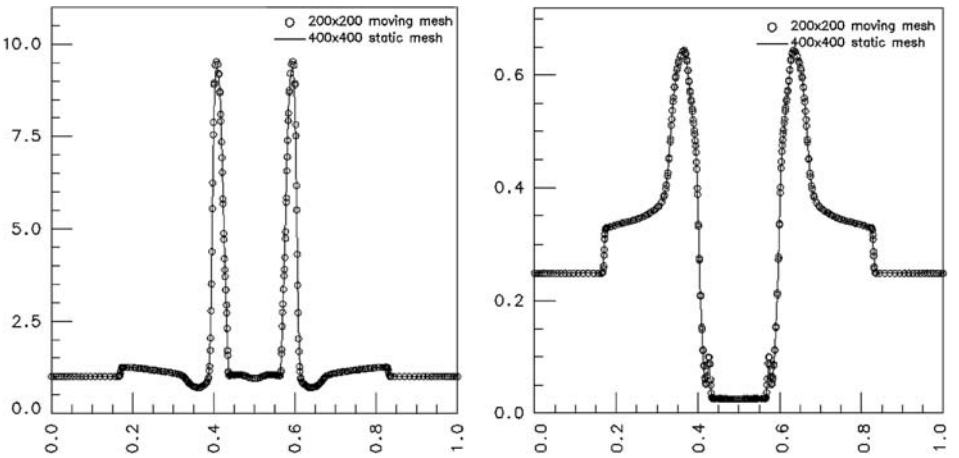

Fig. 10. Same as Fig. 9, except for the second rotor problem.

tions for all four sides. The initial density and velocity are set to unity and zero all over. The initial pressure is set to 0.1 all over except in a central circle of radius 0.1 where it is set to 1000. A magnetic field with a magnitude of $100/\sqrt{4\pi}$ is initialized along the x-direction. We take $\gamma = 1.4$, $\alpha_1 = \alpha_2 = \alpha_3 = 1.0$, and divide Ω_p into 128×128 cells.

Fig. 11 presents the adaptive mesh, contours of the density, pressure, and magnetic pressure at $t = 0.01$, obtained by using the proposed algorithm. We give a comparison of the 2D adaptive mesh solutions ('○') along $x = 0.5$ to corresponding fixed mesh solutions with a resolution of 200×200 uniform cells (solid line) in Fig. 12. The results further show that our adaptive method performs robustly and accurately in the regime of strong waves.

5.6. Cloud–shock interaction

The final example is to solve the cloud–shock interaction problem that has been widely considered in the literatures to model the disruption of a high density cloud by a strong shock wave, see e.g. [17,38,52]. We use set-up of Rossmanith [38]. The computational domain is taken as $[0,1] \times [0,1]$. Supersonic

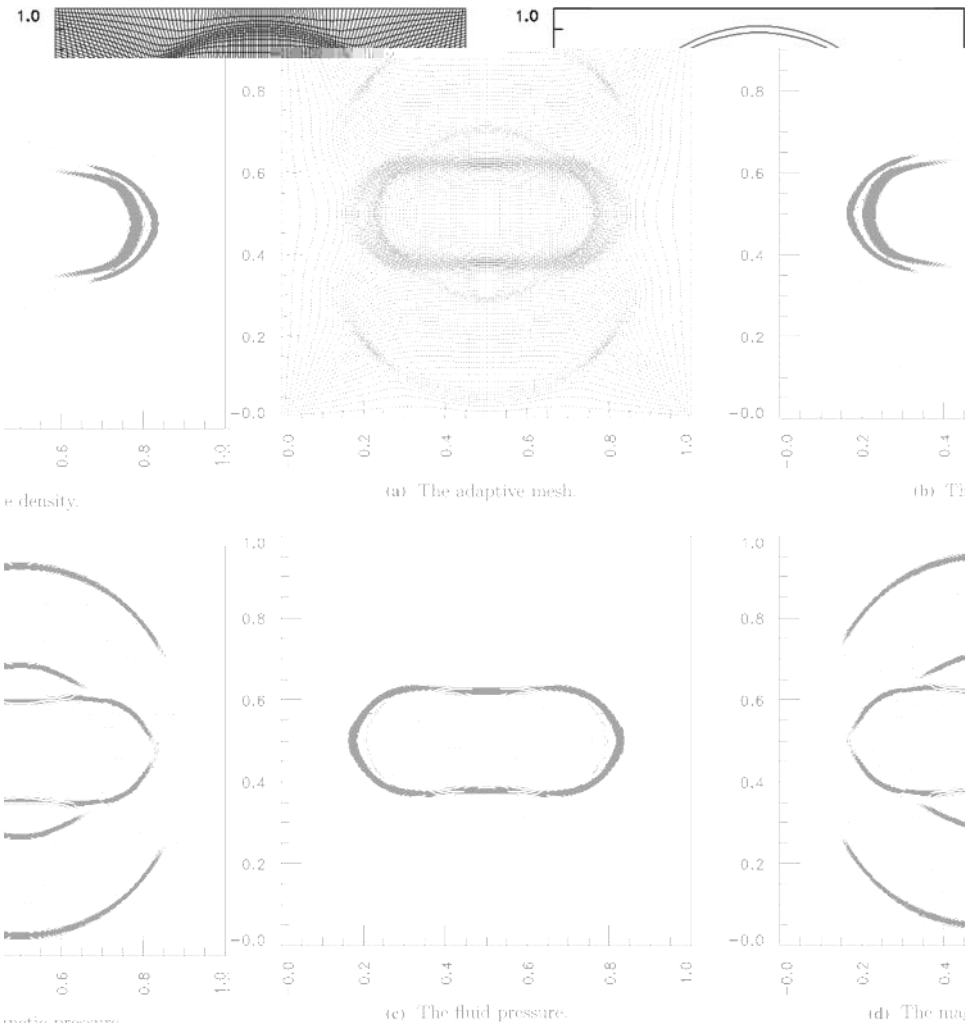

Fig. 11. Solutions to of the stringent blast problem with $N = 128$ at $t = 0.01$. Thirty equally spaced contour lines are taken in the last three graphs.

inflow condition is used on the left, while outflow conditions are specified on others boundaries. The initial data are $(\rho, u_1, u_2, u_3, p, B_1, B_2, B_3) = (3.86859, 11.2536, 0, 0, 167.345, 0, 2.1826182, -2.1826182)$ for $x < 0.05$ and $(\rho, u_1, u_2, u_3, p, B_1, B_2, B_3) = (1, 0, 0, 0, 1, 0, 0.56418985, 0.56418985)$ for $x > 0.05$, which makes a shock located at $x = 0.05$. There is a circular cloud which is in magneto-hydrostatic balance with the surrounding fluid and centered at $\boldsymbol{x} = (0.25, 0.5)$ with a high density $\rho = 10$ and radius $r = 0.15$. The initial magnetic potential $\mathscr{A}$ is given by [38]

$$\mathscr{A}(\boldsymbol{x}, 0) = \begin{cases} -2.1826182x_1 + 0.080921431, & \text{if } x \leqslant 0.05, \\ -0.56418958x_1, & \text{if } x \geqslant 0.05. \end{cases}$$

Fig. 13 shows the adaptive mesh of size 200×200 at $t = 0.06$. Fig. 14 gives schlieren plots of the log of the density and the magnitude of the magnetic field. We see that the reflective pattern is well resolved by the adaptive moving mesh method in comparison with results presented in literatures, e.g. [17,38,52]. Fig. 15 presents further comparison of the adaptive solutions of 200×200 cells and the fixed mesh solutions of 500×500 cells along $y = 0.5$. The results show that the current adaptive algorithm may successfully track and resolve both small, local, and large solution gradients automatically.

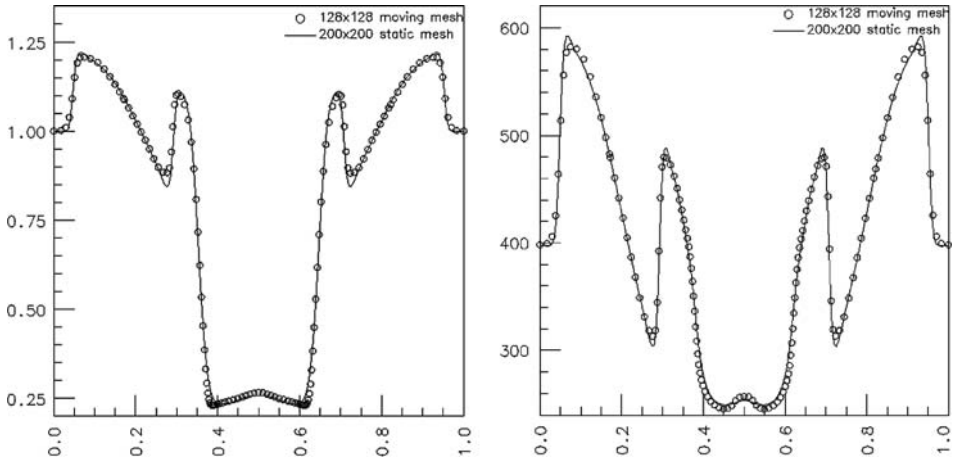

Fig. 12. A comparison of the adaptive mesh solutions ('○') of the blast problem to corresponding fixed mesh solutions with a resolution of 200×200 uniform cells (solid line). Left: the density; right: the magnetic pressure.

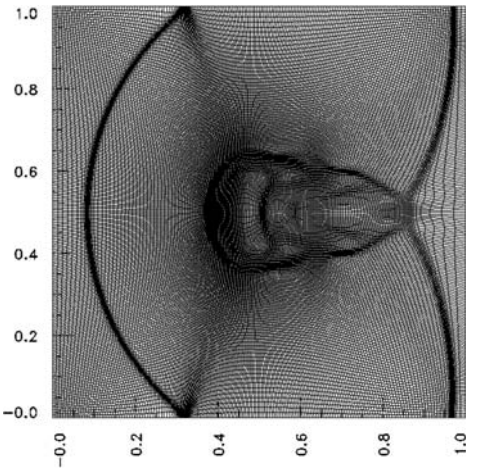

Fig. 13. Adaptive mesh for the cloud–shock interaction problem at time $t = 0.06$ with 200×200 cells.

6. Discussion and conclusion

This paper has developed an adaptive moving mesh algorithm AM^3-2DMHD for two-dimensional ideal magnetohydrodynamics. The algorithm utilizes a staggered constrained transport technique and a magnetic potential to keep the magnetic field divergence-free in each control volume. It consists of two mainly independent parts: MHD evolution and mesh-redistribution. The first part is a high resolution, divergence-free, finite volume scheme on a fixed quadrangular mesh, and the second part is an iterative procedure. In each iteration, mesh points are first redistributed and then the underlying conservative variables (the fluid mass, momentum, and total energy) are updated onto the resulting new meshes by a high-resolution conservative-interpolation formula, while the magnetic potential is re-mapped to the new mesh in a non-conservative way and is reconstructed to give a divergence-free magnetic field on the new mesh.

The main advantages of the proposed method is that both MHD evolution and mesh-redistribution preserve conservation of the underlying numerical solution (the mass, momentum, and total energy) and the divergence-free property of the magnetic field. We have used the proposed algorithm AM^3-2DMHD to solve several well-known MHD problems, which are the smooth Alfvén wave problem, 2D and 2.5D shock tube

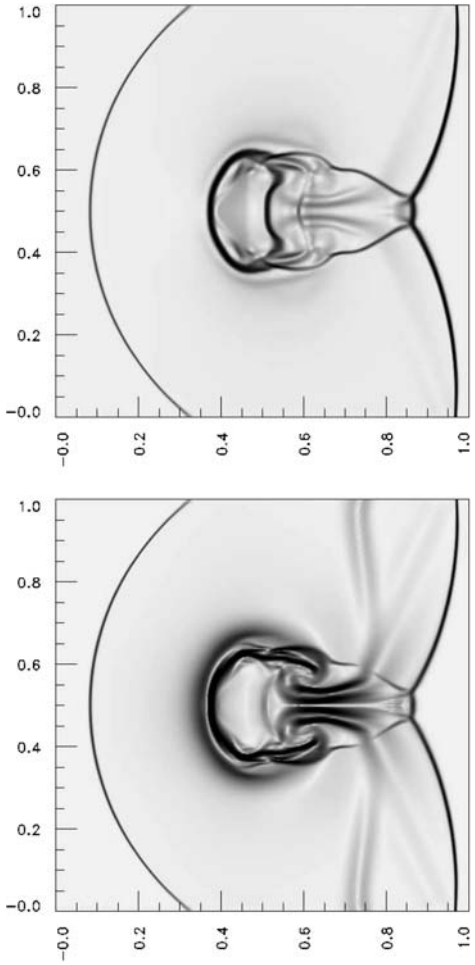

Fig. 14. Schlieren plots of the natural log of the density (top) and magnitude of the magnetic field (bottom) at $t = 0.06$ for the cloud–shock interaction problem.

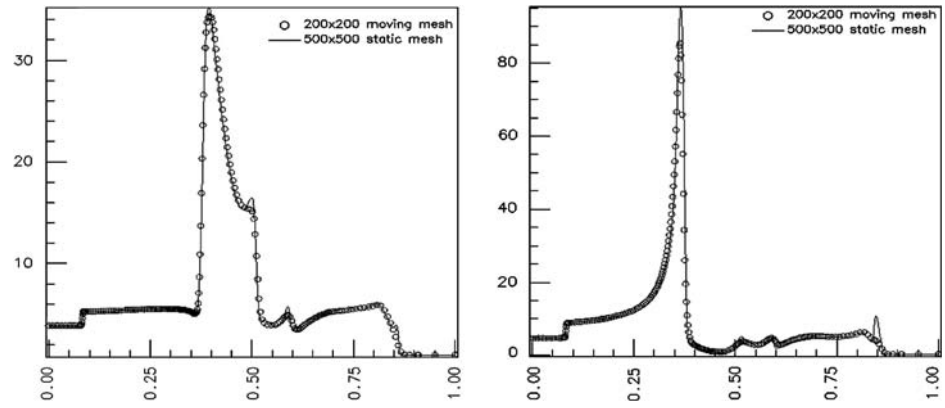

Fig. 15. A comparison of the adaptive solution with a uniform static mesh solution of 500×500 cells along a slab of $y = 0.5$. Left: the density; right: the magnetic pressure.

problems, two rotor problems, the stringent blast problem, and the cloud–shock interaction problem. The results have demonstrated that the algorithm AM^3-2DMHD can achieve second-order numerical accuracy, track and resolve strong shock waves in 2D ideal MHD problems, and preserve conservation and divergence-free property of the physical variables. It is more efficient in obtaining the same resolution with much less number of grid points than the uniform mesh approach. Similar to others moving mesh methods, our algorithm will be very fascinating, when it is applied to the problem whose solutions are very singular in *fairly localized regions*.

Although the proposed algorithm is currently limited to the structured quadrangular mesh and 2D case, we expect to extend it to higher-order accuracy, the unstructured triangular mesh and three-dimensional MHD equations in future.

Acknowledgements

This research was partially supported by the National Basic Research Program under the Grant 2005CB321703, the National Natural Science Foundation of China (Nos. 10431050, 10576001), SRF for ROCS, SEM, and Laboratory of Computational Physics. Authors would also like to thank the anonymous referees for the detailed reports that helped to improve the manuscript.

References

[1] N. Aslan, MHD-A: a fluctuation splitting wave model for planar magneto-hydrodynamics, J. Comput. Phys. 153 (1999) 437–466.
[2] B.N. Azarenok, Variational barrier method of adaptive grid generation in hyperbolic problems of gas dynamics, SIAM J. Numer. Anal. 40 (2002) 651–682.
[3] B.N. Azarenok, S.A. Ivanenko, Application of adaptive grids in numerical analysis of time-dependent problems in gas dynamics, Comput. Maths. Math. Phys. 40 (2000) 1330–1349.
[4] B.N. Azarenok, T. Tang, Second-order Godunov-type scheme for reactive flow calculations on moving meshes, J. Comput. Phys. 206 (2005) 48–80.
[5] D.S. Balsara, Divergence-free adaptive mesh refinement for magnetohydrodynamics, J. Comput. Phys. 174 (2001) 614–648.
[6] D.S. Balsara, Second order accurate schemes for magnetohydrodynamics with divergence-free reconstruction, Astrophys. J. Suppl. 151 (2004) 149–184.
[7] D.S. Balsara, D.S. Spicer, A staggered mesh algorithm using high order Godunov fluxes to ensure solenoidal magnetic fields in magnetohydrodynamics simulations, J. Comput. Phys. 149 (1999) 270–292.
[8] P. Bochev, M. Shashkov, Constrained interpolation (remap) of divergence-free field, Comput. Methods Appl. Mech. Engrg. 194 (2005) 511–530.
[9] J.U. Brackbill, An adaptive grid with directional control, J. Comput. Phys. 108 (1993) 38–50.
[10] J.U. Brackbill, D.C. Barnes, The effect of nonzero div**B** on the numerical solution of the magnetohydrodynamic equations, J. Comput. Phys. 35 (1980) 426–430.
[11] J.U. Brackbill, J.S. Saltzman, Adaptive zoning for singular problems in two dimensions, J. Comput. Phys. 46 (1982) 342–368.
[12] M. Brio, C.C. Wu, An upwind differencing schemes scheme for the equations of ideal magnetohydrodynamic equations, J. Comput. Phys. 75 (1988) 400–422.
[13] W.M. Cao, W.Z. Huang, R.D. Russell, An *r*-adaptive finite element method based upon moving mesh PDEs, J. Comput. Phys. 149 (1999) 221–244.
[14] H.D. Ceniceros, T.Y. Hou, An efficient dynamically adaptive mesh for potentially singular solutions, J. Comput. Phys. 172 (2001) 609–639.
[15] D.A. Clarke, A search for the effects of active magnetic fields in extra-galactic radio sources, Ph.D. Thesis, New Mexico University, Albuquerque, 1988.
[16] J-P Croisille, R. Khanfir, G. Chanteur, Numerical simulation of the MHD equations by a kinetic-type method, J. Sci. Comput. 18 (1995) 481–492.
[17] W.L. Dai, P.R. Woodward, A simple finite difference scheme for multi-dimensional magnetohydrodynamical equations, J. Comput. Phys. 142 (1998) 331–369.
[18] W. Dai, P.R. Woodward, A high-order Godunov-type scheme for shock interactions in ideal magnetohydrodynamics, SIAM J. Sci. Comput. 18 (1997) 957–981.
[19] S.F. Davis, J.E. Flaherty, An adaptive finite element method for initial-boundary value problems for partial differential equations, SIAM J. Sci. Stat. Comput. 3 (1982) 6–27.
[20] Y.N. Di, R. Li, T. Tang, P.W. Zhang, Moving mesh finite element methods for the incompressible Navier–Stokes equations, SIAM J. Sci. Comput. 26 (2005) 1036–1056.
[21] A.S. Dvinsky, Adaptive grid generation from harmonic maps on Riemannian manifolds, J. Comput. Phys. 95 (1991) 450–476.

[22] C.R. Evans, J.F. Hawley, Simulation of magnetohydrodynamic flows – a constrained transport method, Astrophys. J. 332 (1988) 659–677.
[23] R. Fazio, R. LeVeque, Moving-mesh methods for one-dimensional hyperbolic problems using CLAWPACK, Comput. Math. Appl. 45 (2003) 273–298.
[24] A. Harten, J.M. Hyman, Self-adjusting grid methods for one-dimensional hyperbolic conservation laws, J. Comput. Phys. 50 (1983) 235–269.
[25] G.S. Jiang, C.C. Wu, A high-order WENO finite difference scheme for the equation of ideal magnetohydrodynamics, J. Comput. Phys. 150 (1999) 561–594.
[26] O.S. Jones, U. Shumlak, D.S. Eberhardt, An implicit scheme for nonideal magnetohydrodynamics, J. Comput. Phys. 130 (1997) 231–242.
[27] S.T. Li, An HLLC Riemann solver for magneto-hydrodynamics, J. Comput. Phys. 203 (2005) 344–357.
[28] S.T. Li, H. Li, A novel approach of divergence-free reconstruction for adaptive mesh refinement, J. Comput. Phys. 199 (2004) 1–15.
[29] S. Li, L. Petzold, Moving mesh methods with upwinding schemes for time-dependent PDEs, J. Comput. Phys. 131 (1997) 368–377.
[30] R. Li, T. Tang, P.W. Zhang, Moving mesh methods in multiple dimensions based on harmonic maps, J. Comput. Phys. 170 (2001) 562–588.
[31] R. Li, T. Tang, P.W. Zhang, A moving mesh finite element algorithm for singular problems in two and three space dimensions, J. Comput. Phys. 177 (2002) 365–393.
[32] F. Liu, S. Ji, G. Liao, An adaptive grid method and its application to steady Euler flow calculations, SIAM J. Sci. Comput. 20 (1998) 811–825.
[33] K. Miller, R.N. Miller, Moving finite element. I, SIAM J. Numer. Anal. 18 (1981) 1019–1032.
[34] R.S. Myong, P.L. Roe, On Godunov-type schemes for magnetohydrodynamics. I. A model system, J. Comput. Phys. 147 (1998) 545–567.
[35] K.G. Powell, An approximate Riemann solver for magnetohydrodynamics (that works in more than one dimensions), ICASE Report No. 94-24, Langley, VA, 1994.
[36] K.G. Powell, P. Roe, T. Linde, T.I. Gombosi, D.L. DeZeeuw, A solution-adaptive upwind scheme for ideal magnetohydrodynamics, J. Comput. Phys. 154 (1999) 284–309.
[37] W.Q. Ren, X.P. Wang, An iterative grid redistribution method for singular problems in multiple dimensions, J. Comput. Phys. 159 (2000) 246–273.
[38] J.A. Rossmanith, A high-resolution constrained transport method with adaptive mesh refinement for ideal MHD, Comput. Phys. Commun. 164 (2004) 128–133.
[39] D. Ryu, T.W. Jones, A. Frank, Numerical magnetohydrodynamics in astrophysics: Algorithm and tests for multi-dimensional flow, Astrophys. J. 452 (1995) 785–796.
[40] K. Saleri, S. Steinberg, Flux-corrected transport in a moving grid, J. Comput. Phys. 111 (1994) 24–32.
[41] D.D. Schnack, I. Lottati, Z. Mikie, P. Satyanarayana, A finite-volume algorithm for three-dimensional magnetohydrodynamics on an unstructured adaptive grid in axially symmetric geometry, J. Comput. Phys. 140 (1998) 71–121.
[42] C.-W. Shu, S. Osher, Efficient implementation of essentially non-oscillatory shock capturing schemes, J. Comput. Phys. 77 (1988) 439–471.
[43] J.M. Stockie, J.A. Mackenzie, R.D. Russell, A moving mesh method for one-dimensional hyperbolic conservation laws, SIAM J. Sci. Comput. 22 (2001) 1791–1813.
[44] H.R. Strauss, D.W. Longcope, An adaptive finite element method for magnetohydrodynamics, J. Comput. Phys. 147 (1998) 318–336.
[45] Z.-J. Tan, Z.-R. Zhang, Y.-Q. Huang, T. Tang, Moving mesh methods with locally varying time steps, J. Comput. Phys. 200 (2004) 347–367.
[46] T. Tanaka, Finite volume TVD scheme on an unstructured grid system for three-dimensional MHD simulations of inhomogeneous systems including strong background potential field, J. Comput. Phys. 111 (1995) 81–92.
[47] H.Z. Tang, T. Tang, Adaptive mesh methods for one- and two-dimensional hyperbolic conservation laws, SIAM J. Numer. Anal. 41 (2003) 487–515.
[48] H.Z. Tang, T. Tang, P.W. Zhang, An adaptive mesh redistribution method for nonlinear Hamilton–Jacobi equations in two- and three-dimensions, J. Comput. Phys. 188 (2003) 543–572.
[49] H.Z. Tang, K. Xu, A high-order gas-kinetic method for multidimensional ideal magnetohydrodynamics, J. Comput. Phys. 165 (2000) 69–88.
[50] T. Tang, Moving mesh methods for computational fluid dynamics, Contemp. Math. 383 (2005) 141–174.
[51] E.F. Toro, Riemann Solvers and Numerical Methods for Fluid Dynamics, A Practical Introduction, Springer, 1999.
[52] G. Tóth, The $\nabla \cdot B = 0$ constraint in shock-capturing magnetohydrodynamics codes, J. Comput. Phys. 161 (2000) 605–652.
[53] G. Tóth, D. Odstrcil, Comparison of some flux corrected transport and total variation diminishing numerical schemes for hydrodynamic and magnetohydrodynamic problems, J. Comput. Phys. 128 (1996) 82–100.
[54] B. van Leer, Towards the ultimate conservative difference schemes V. A second-order sequel to Godunov's method, J. Comput. Phys. 32 (1979) 101–136.
[55] D.S. Wang, X.P. Wang, Three dimensional adaptive method based on iterative grid redistribution, J. Comput. Phys. 199 (2004) 423–436.
[56] A. Winslow, Numerical solution of the quasi-linear Poisson equation, J. Comput. Phys. 1 (1967) 149–172.
[57] K. Xu, Gas-kinetic theory based flux splitting method for ideal magnetohydrodynamics, J. Comput. Phys. 153 (1999) 334–352.
[58] A. Zachary, A. Malagoli, P. Colella, A high-order Godunov method for multidimensional ideal magnetohydrodynamics, SIAM J. Sci. Comput. 15 (1994) 263–284.